UNIVERSITY OF BIRMINGHAM
University of Birmingham Research at Birmingham

Enabling high efficiency magnetic refrigeration using laser powder bed fusion of porous $LaCe(Fe,Mn,Si)_{13}$ structures

Hussein, Abdelmoez; Sheridan, Richard; Attallah, Moataz; Jeong, Minki

DOI:
10.1016/j.addma.2022.102620

License:
Creative Commons: Attribution-NonCommercial-NoDerivs (CC BY-NC-ND)

Document Version
Peer reviewed version

Citation for published version (Harvard):
Hussein, A, Sheridan, R, Attallah, M & Jeong, M 2022, 'Enabling high efficiency magnetic refrigeration using laser powder bed fusion of porous $LaCe(Fe,Mn,Si)_{13}$ structures', *Additive Manufacturing*, vol. 51, 102620. https://doi.org/10.1016/j.addma.2022.102620

Link to publication on Research at Birmingham portal

General rights
Unless a licence is specified above, all rights (including copyright and moral rights) in this document are retained by the authors and/or the copyright holders. The express permission of the copyright holder must be obtained for any use of this material other than for purposes permitted by law.

•Users may freely distribute the URL that is used to identify this publication.
•Users may download and/or print one copy of the publication from the University of Birmingham research portal for the purpose of private study or non-commercial research.
•User may use extracts from the document in line with the concept of 'fair dealing' under the Copyright, Designs and Patents Act 1988 (?)
•Users may not further distribute the material nor use it for the purposes of commercial gain.

Where a licence is displayed above, please note the terms and conditions of the licence govern your use of this document.

When citing, please reference the published version.

Take down policy
While the University of Birmingham exercises care and attention in making items available there are rare occasions when an item has been uploaded in error or has been deemed to be commercially or otherwise sensitive.

If you believe that this is the case for this document, please contact UBIRA@lists.bham.ac.uk providing details and we will remove access to the work immediately and investigate.

Download date: 26. Apr. 2024

Enabling High Efficiency Magnetic Refrigeration using Laser Powder Bed Fusion of Porous $LaCe(Fe,Mn,Si)_{13}$ Structures

Abd El-Moez A. Mohamed[a], Minki Jeong[b], Richard S. Sheridan[a], Moataz M. Attallah[*a]

a: School of Metallurgy and Materials, University of Birmingham, B15 2TT, Birmingham, United Kingdom

b: School of Physics and Astronomy, University of Birmingham, B15 2TT, Birmingham, United Kingdom

*Corresponding author: M. M. Attallah (m.m.attallah@bham.ac.uk)

Abstract

The aim of this study is to assess the processability of the $LaCe(Fe,Mn,Si)_{13}$ magnetocaloric material using laser powder bed fusion (LPBF) to create room temperature high surface-area-to-volume magnetic refrigeration media. LPBF process optimisation was performed on block samples, focusing on the build densification and the microstructural development. The porosity fraction decreased with the increase in laser energy density (E), however, cracks and keyholes were induced at $E \geq 140 J/mm^3$. Following thermal heat treatment and quenching, the magnetic entropy change (ΔS) of the blocks increased with the increase in E, due to the increase in homogeneity, where the maximum value achieved at a Curie temperature (T_c) of ~290K for the sample built using $E=123 J/mm^3$ was 4.9J/kg.K. Meanwhile, the samples built using $E>140 J/mm^3$ showed higher ΔS_{max} values that reaches 7.2J/kg.K but at lower T_c of 260K and the samples are rich in cracks. The block sample built using $E=123 J/mm^3$ is recommended as the optimum condition, where it shows the lowest defects and the highest room temperature ΔS with highest compressive mechanical stress value of 90MPa. A microchannel block sample was built using the optimum condition, which shows ΔS_{max} value of 4.2J/kg.K with adiabatic temperature change of 1.4K at $\mu_0 H=1T$, which is close to the value of the block sample revealing the consistency in the magnetocaloric properties between the block and the porous samples.

Keywords: Laser powder bed fusion; La-Fe-Si alloys; Microstructure; Magnetic properties; Magnetic refrigeration

1. Introduction

Traditional gas compression cooling (GCC) technology have generally poor Carnot cycle efficiency (typically ~10%) [1], over and above the polluting gas emissions, such as carbon dioxide and fluorocarbons [2]. The lower efficiency and the harmful environmental effects of GCC technologies have increased the interest in identifying more efficient and environmentally friendly alternatives. Magnetic refrigeration (MR) is a novel cooling

technology, which addresses both the previous concerns, achieving ~60% Carnot cycle efficiency [3] without any gas emissions. MR is based on the magnetocaloric effect (MCE), which occurs in a special magnetic material that shows high change in the magnetic entropy (ΔS) under the effect of an externally applied magnetic field. Rare earth-based alloys have been investigated and reported as the largest MCE materials, in addition to Gd, which has been set as the benchmark in MR technology [4]. However, some concerns have been raised which hinder their usage, such as their high cost, poor corrosion resistance, toxicity, and lack of availability [2], making it necessary to develop alternative sustainable and efficient alloys.

$La(Fe,Si)_{13}$ based alloys have been reported as a giant magnetic refrigerant [5] with higher thermal conductivity (11.6W/mK), lower costs and non-toxic effects [6]. The giant MCE in these alloys refers to the first order itinerant electron metamagnetic (IEM) ferromagnetic-paramagnetic (FM-PM) transition, which is associated with a change in the band structure of the 3d orbital [7]. According to previous studies, the $La(Fe,Si)_{13}$ cast alloy shows T_c around 195K and ΔS values of 19J/kg.K at $\mu_0 H$=1T, which can be improved to 29J/kg.K by the partial substitution of La by Ce at the same value of the applied magnetic flux density [8]. In addition, the partial substitution of Fe by Mn decreases the T_c and the MCE [9]. Despite the giant MCE properties of the $La(Fe,Si)_{13}$ alloy, there are two important challenges, which restrict their usage in real applications: their low T_c [6,10] and low ductility and strength [11]. The T_c value could be shifted towards room temperature via two ways: the partial substitution of Fe by Co atoms [11] or introducing interstitial atoms, such as H or C [12]. However, in the first case, the MCE properties are suppressed [13]. The weak mechanical strength of the $La(Fe,Si)_{13}$ based alloys (120 MPa) do not allow for the shaping of it into prototypes via traditional techniques, such as direct machining [14] and epoxy bonding [15], as the bulk material is cracked during direct machining and the MCE is weakened by the non-magnetic elements in epoxy bonding. Shoa *et al.* reported an improvement in the mechanical strength of the $La(Fe,Si)_{13}$ alloy through excess α-Fe, however, this is also associated with large suppression of the MCE properties [16]. From the applications viewpoint, one of the typical problems in active magnetic refrigeration is the heat transfer time between the magnetocaloric material and the fluid in heat exchangers (the materials is not being exposed to significant external loads during the process beyond the thermal loads). One way to reduce this time, thereby increasing the efficiency, is to increase the magnetic refrigerant surface area by shaping it into a porous structure [11], which is difficult to achieve using the traditional methods.

Additive manufacturing (AM) technologies allow the manufacturing of complex shapes with high precision and have been used previously to process several magnetic materials such as Ni-Fe-Mo [17], CoFeNi [18], Fe-Ni [19], Fe-Si [20] and functionally graded CoFe-NiFe [21] soft magnets and NdFeB hard magnets [22], where high microstructural density was observed. Other few works on additive manufacturing of magnetic materials have been summarised in [23]. Moore *et al.* performed a trial to produce 3D printed wavy channel block and fin-shaped rods of the $La(Fe,Co,Si)_{13}$ alloy using the laser powder bed fusion (LPBF) process [11]. Despite the results being somewhat positive, it lacked the microstructure-MCE properties correlations, which should help rationalise the obtained results. The current study fills this blank by investigating the relationship between the microstructural development and build density of LPBF-processed $LaCe(Fe,Mn,Si)_{13}$ blocks and their respective MCE properties. The aim of this study is to produce dense 3D printed $LaCe(Fe,Mn,Si)_{13}$, as well as porous designed prototypes with high room temperature MCE performance. This objective is conducted via achieving optimal build density, microstructure, and MCE properties of blocks, microchannel blocks, and lattice strut samples. To correlate the build integrity and microstructure and the MCE performance, the results of the LPBF-processed samples are compared with powder hot isostatic pressing (HIP) of the same alloy consolidated to full density.

2. Experimental

2.1 Powder characterisation

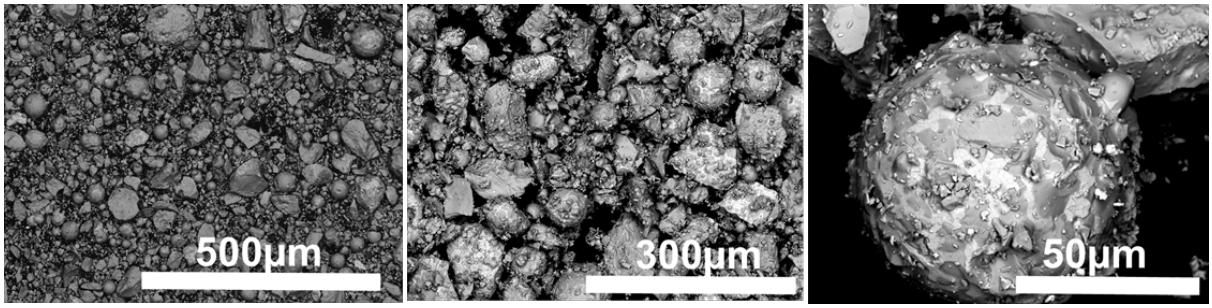

Fig.1: SEM micrographs showing the morphology of the starting raw pre-alloyed $LaCe(Fe,Mn,Si)_{13}$ powder.

Gas atomised $LaCe(Fe,Mn,Si)_{13}$ pre-alloyed powder was provided by Erasteal with the chemical composition shown in Table 1, argon gas was used during the atomisation process. The powder morphology in Fig.1 shows a distribution of spherical and irregular shaped particles with satellites, suggesting a low flowability. The powder did not flow when tested

using the hall flow test. This undesired morphology is quite common even when gas atomisation is used for this alloy [11]. The powder was sieved to a 63 µm mesh.

Table 1: Chemical composition analysis in wt.% of the pre-alloyed powder and as-fabricated LPBF block E=123J/mm^3, E=183J/mm^3 and E=278/mm^3 samples. Also the oxygen analysis of the block sample E=123J/mm^3 after hydrogenation is included.

	La	Ce	Si	Mn	Fe	H (ppm)	Oxygen (ppm)	<0.02
Powder	12.79	5.50	4.61	1.33	Bal	1629	1291	Traces
Block E=123 J/mm^3	11.94	5.31	4.41	1.02	Bal	176	1350	Traces
Block E=183 J/mm^3	10.45	4.88	4.32	0.96	Bal	132	1376	Traces
Block E=278 J/mm^3	9.83	4.01	3.98	0.53	Bal	153	1458	Traces
Block E=123J/mm^3 H	-	-	-	-	-		1125	

2.2 Sample fabrication

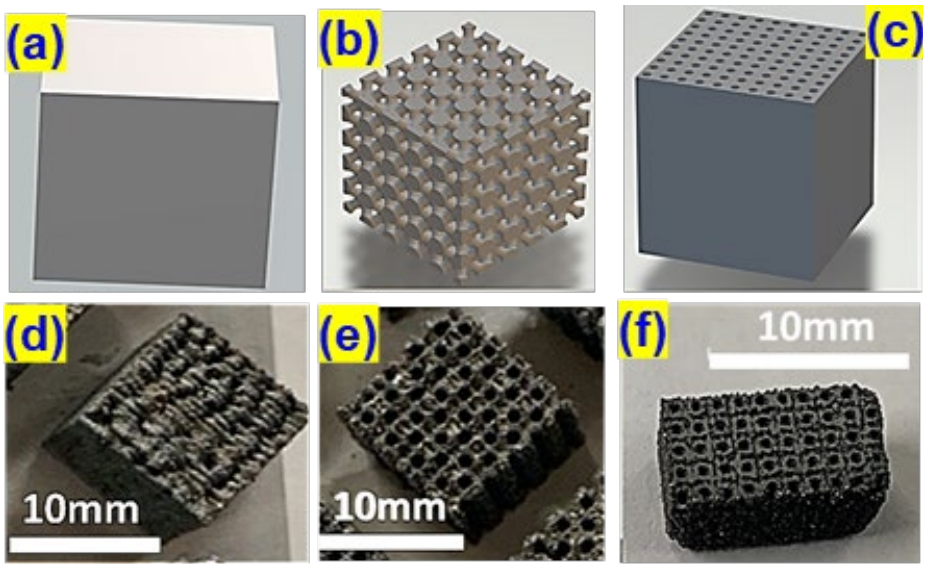

Fig.2: (a,b,c) CAD designs of blocks, strut lattice and microchannel blocks geometries, respectively, and (d,e,f) the respective 3D printed samples.

Bulk samples were built using LPBF technique on top of a steel substrate using a Concept Laser M2 Cusing system in Argon atmosphere controlled to <1000 ppm of O_2, with laser spot size of 67µm. The set-up is presented in supplementary (S) Fig.S1 with a picture of the powder bed. Three different designs of 10x10x10mm^3 were built; blocks, body centred cubic (BCC) strut-based lattice structure, and porous blocks with straight microchannels (MC

blocks), as per the designs in Fig. 2a-c with their respective fabricated parts in Fig.2d-f, respectively. The porous structures represent some typical designs that can be used in magnetic refrigeration, to maximise the heat transfer via the flow of the cooling fluid (typically water) through the channels. The BCC strut lattice structure was designed with a unit cell dimension of 2mm, a strut thickness of 0.5mm and a strut length of 0.5mm. The MC blocks were designed with a MC diameter of 0.5mm (500µm), with a separation distance of 0.5mm. The optimisation process for maximum densification was performed on blocks using the parametric combinations detailed in Table 2 with different laser scanning strategies (unidirectional, island and chess), as illustrated in the schematic figure in the supplementary data (Fig.S2).

Table2: The investigated LPBF processing parameters.

Laser Power (W)	Scan Speed (mm/s)	Scan spacing (mm)	Volume Energy density (J/mm^3)
150-300	450-1800	0.045-0.09	31-493

Design of experiment (DOE) was applied for the density optimisation of the MC blocks. Meanwhile, a different combination of the same DOE was applied to optimise the integrity of the lattice structure. The laser energy density model was used to describe the specific heat input within the optimisation process, which is given by Equation 1 [23], where E is the laser volumetric energy density (J/mm^3), P is the laser power (W), v is the scanning speed (mm/s), h is the laser hatch spacing (mm), and t is the layer thickness.

$$E=P(Watt)/[v(mm/s).h(mm).t(mm)] \quad (1)$$

The as-fabricated (AF) LPBF samples were encapsulated in Argon filled quartz ampoules and given a heat treatment (HT) below the melting temperature (1420 °C, according to the material data sheet), which is close to the melting point of La-Fe-Si-Co (1527°C) [11]. The furnace temperature was ramped up by 10ºC/min and held at 1050ºC for 168 hours, followed by oil quenching. The as-quenched (AQ) samples were followed by another thermal HT at 400˚C for 6 hours in hydrogen atmosphere in a tube furnace; with the hydrogen-treated samples being referred to as HQ. The furnace tube was filled with hydrogen gas with one-bar pressure; the temperature was ramped up by 10ºC/min to 400˚C and held for 6 hours before the temperature was ramped down back by 10ºC/min to room temperature. Finally, a mild steel canister was filled with the as-received powder (particle size ≤63µm) in an inert atmosphere, outgassed, seal welded and HIPed at 1160˚C and 120MPa for 4 hours (referred to hereafter as powder HIP).

2.3 Microstructure characterisation and magnetic measurements

The AF LPBF samples were cut from the substrate using an automatic cutting saw with a diamond wheel and an oil-based lubricant to prevent corrosion. The samples were sectioned along the build direction (BD), mounted in Bakelite, ground, and polished to oxide polishing finish. The microstructure was characterised using a Hitachi TM3000 back scattering scanning electron microscope (SEM) and a Brunel optical microscope. The chemical composition was determined using x-ray fluoresce (XRF) for Ce and La, inductively coupled plasma (ICP) for Fe,Mn,Si and Lab Equipment corporation (LECO) for Oxygen and Hydrogen. The sample density was assessed using the Archimedes method (OHAUS adventurer analytical balance) [24]. The porosity fraction quantitative analysis was performed via image analysis of the 9 optical micrographs, covering an area of 8mm×8mm, using ImageJ software. Few optical images are presented in Fig.S3 as an example.

Statistical analysis were performed using Design Expert software. The crystal structure and phase identification were performed by X-ray diffraction (XRD) using a Bruker D2 Phaser XRD diffractometer (Co K_α radiation, λ=1.79Å) and the crystal structure analysis was performed via Rietveld refinement using Fullprof software. The characterisation in the first-round optimisation was conducted on the block samples. Microhardness measurements were performed along the BD using a Wilson VH1102-1202 microhardness tester, where each data point is an average of 16 readings. The used load was 25g with indentation dimension of 10.7µm ±0.3. Differential scanning calorimetry (DSC) traces were recorded using Mettler Toledo DSC model in temperatures range between 255 and 330K, for samples (~25 mg) cycled at heating rates of 10 K/min under argon. Mechanical compression test was performed on 10x10x10mm^3 coupons using a Zwick Roell 1484 universal testing machine.

Magnetic measurements for the AQ and HQ samples (along the LPBF BD) were performed using a superconducting quantum interference device (SQUID) magnetometer magnetic properties measurements system. The temperature dependence of magnetisation curves, M(T), were measured at μ_0H=0.01T within a temperature range between 100 and 350K. The M(T) curve of the AF-LPBF sample was measured using a Lakeshore7300 VSM, due to its high temperature capability (300K-1173K). The isothermal magnetisation curves, M(H), were measured in temperatures ranging between 220 and 350K under μ_0H=1T, with temperature intervals of 10K. The MCE was determined in terms of the magnetic entropy change (ΔS), which was calculated from the M(H) curves using Maxwell's relation (Eq.2). The adiabatic temperature change (ΔT_{ad}) was measured directly according to DIN SPEC

91373-2, where the sample is fitted in a cryogenic system and then the temperature is set to a certain value. A magnetic field of 1T is then applied and removed across the sample and the change in sample's temperature is measured using and this step is repeated at different values of temperatures.

$$\Delta S(T,H)=\int_0^H (\frac{\delta M}{\delta T})_H \, dH \qquad (2)$$

3. Results and discussion

3.1 Microstructure

In LPBF, the process parameters are one of the factors that affect the microstructure of the processed material because of the associated defects such porosity and cracks [25]. It has been reported that such defects can affect the associated properties such as mechanical and magnetic properties [21]. This section will discuss the influence of process parameter and laser scanning strategies on microstructure density of blocks, microchannel blocks, and lattices to achieve dense components.

3.1.1 Microstructure of the AF block samples

Fig.3a,b shows the densification dependence on E, in terms of porosity fraction and Archimedes density (without open porosity), respectively, for the AF block samples. The Archimedes density shows a gradual increase with increasing E, due to the decrease in porosity fraction, reaching a consolidation threshold at E_{th}=100J/mm^3 with an average density onset value of 6.8g/cm^3 (the estimated theoretical density is 7.72 g/cm^3). This is a typical consolidation behaviour of the LPBF process [25], and the E_{th} value is like the reported levels of other LPBF processed magnetic materials, such as La(Fe,Co,Si)$_{13}$ [11] and Ni-Fe-Mo [26] alloys. The average maximum density value is consistent with the previously reported values of sintered La(Fe,Si)$_{13}$ (7.2g/cm^3) [27] and the cast La (Fe,Si)$_{13}$ (7.11g/cm^3) alloys [14]. It is worth mentioning that the low density at low E values can be attributed to the laser process parameters as powder was spread well on the powder bed [28]. The microstructural density changes insignificantly with the change in laser scanning strategy, as shown by the Archimedes density in Fig.3c. For example, the difference in the density value of the samples built with E≥103J/mm^3 at the three scanning strategies ≈0.2g/cm^3, so all primary investigations for the blocks have been conducted on the unidirectional (non-rotating) laser scanned samples. Despite the densification dependence on E, E is a combination of several laser parameters, as expressed by Eq.1. A full factorial design was constructed to investigate the significance of each individual factor on porosity with statistical data analysis listed in Table S1.

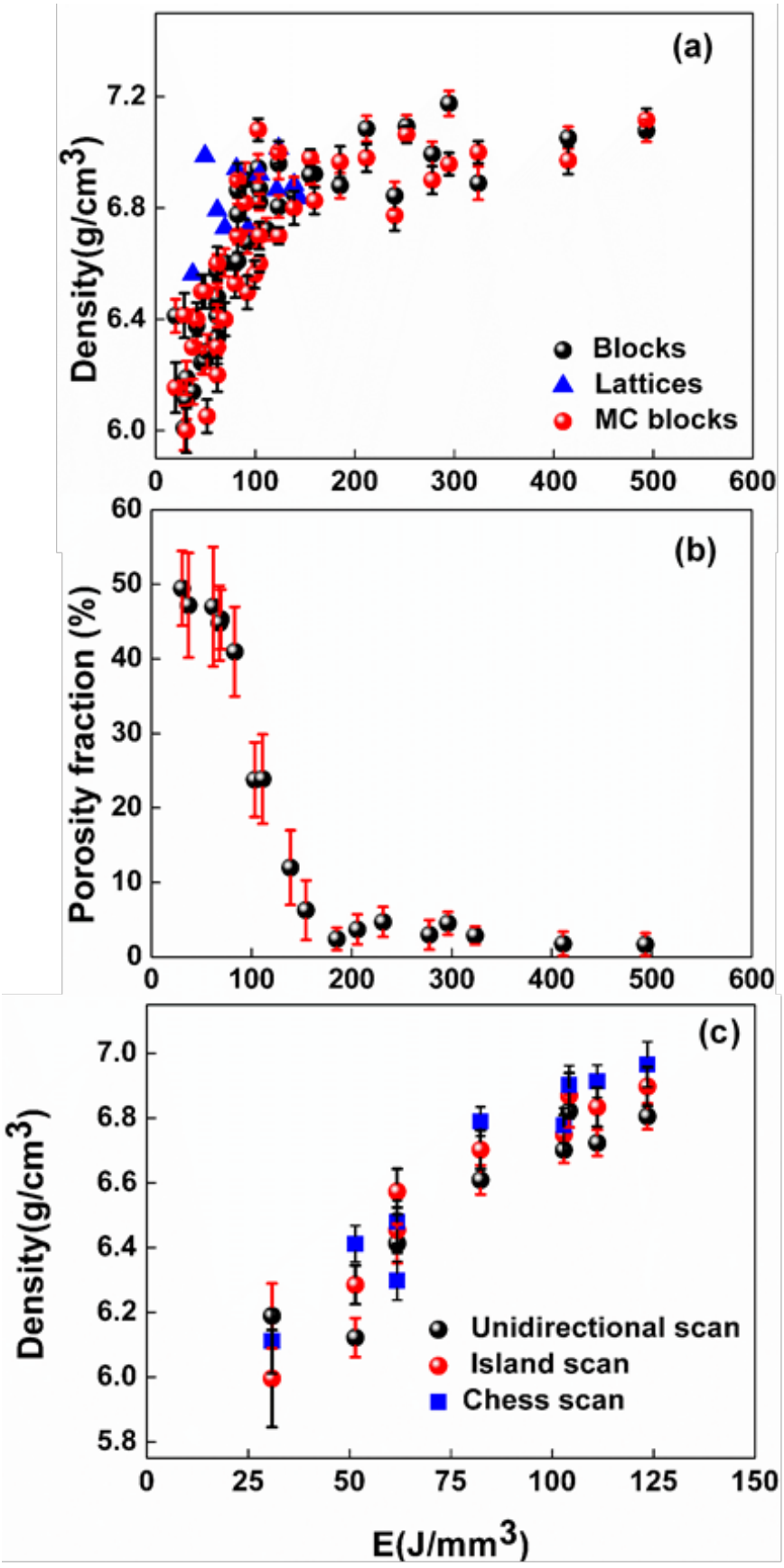

Fig.3 : (a,b) The influence of E on density, porosity fraction, and (c) the influence of laser scanning strategy on density.

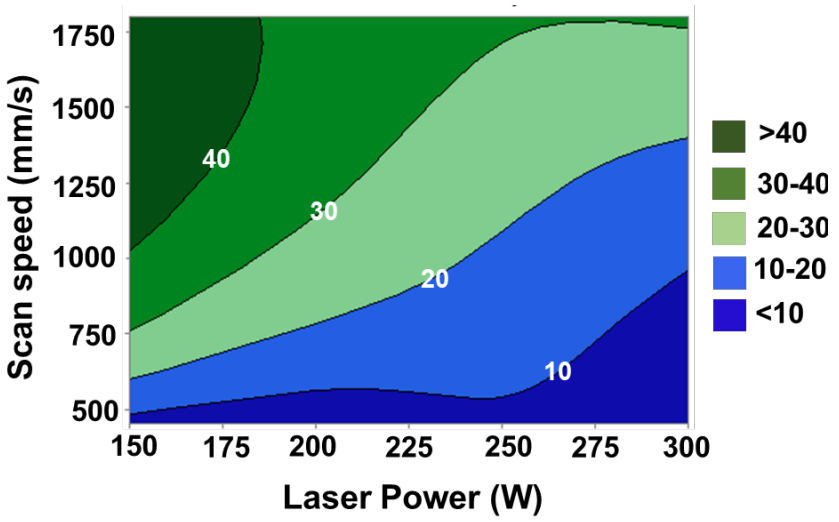

Fig.4: Contour plot of porosity fraction with respect to laser power and scan speed.

The fitting model is selected based on several criteria, such as not being aliased, the highest fitting statistic parameters R^2 (closest to unity), the difference between the predicted R^2 & the adjusted R^2 not being more than 0.2, the significance of model ordering (P-value <0.05) and the insignificance of a lack of fit (>0.1) [29, 30]. Based on these criteria, the analysis of variance (ANOVA) (Table S2) shows the linear model as the best fitting model with the experimental porosity data, where the individual effect of parameters and the possible interactions are plotted in Fig.S4 and indicates the influence of all laser parameters on porosity.

Fig.4 reveals higher laser power and slower scanning speed should be considered to reduce porosity. Such suggestions have the effect of increasing E to the processed alloy, allowing for a high degree of consolidation. The predicted processing parameters which should be considered for maximum build density (≈0.3% porosity fraction) are a laser power of 297W, a scan speed of 522mm/s and a hatch spacing of 0.065mm, which correspond to a specific energy input value of E=293J/mm^3.

3.1.2 Microstructure evolution and defects mechanism

The SEM micrographs in Fig.5 a-f of AF selected block samples provide evidence for the microstructural evolution with increasing E; additional micrographs are available in Fig.S5. The samples built with lower E (lower P and higher V) show un-melted particles within the builds (lack of fusion defects) which results in lower microstructural density. The monotonic increase in E decreases the lack of fusion defects and increases the degree of consolidation, which consistent with the suggested assumptions made by the linear model. Cracks and

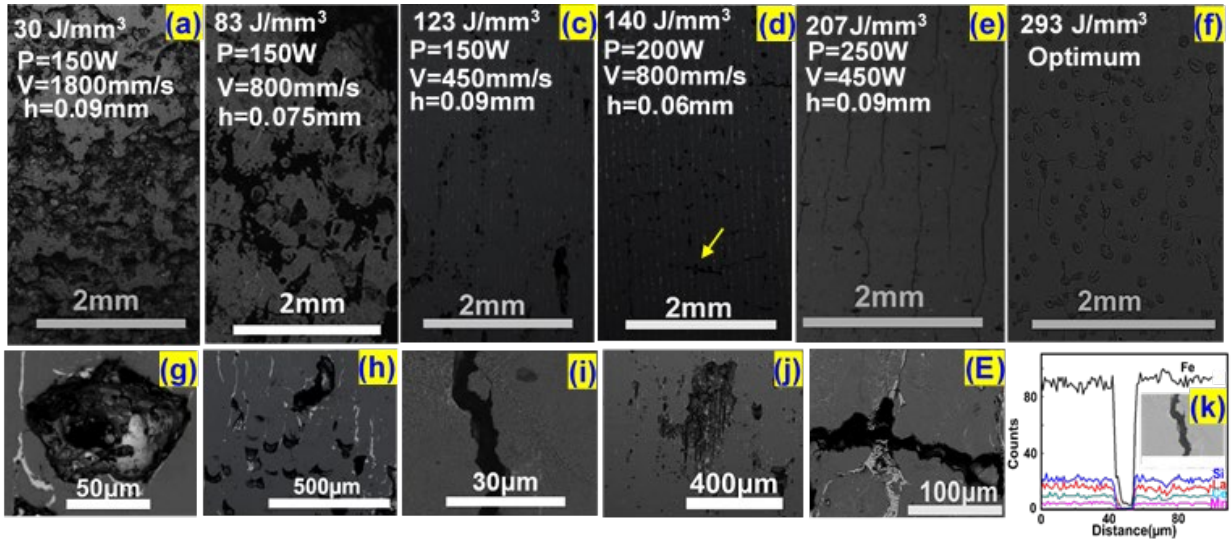

Fig.5: (a,b,c,d,e) SEM micrographs showing the influence of LPBF processing parameters on the build density, (f) the SEM of the optimum condition predicted by the linear model, high magnification SEM for (a) the lack of fusion, (h) evaporation, (I,j,E) typical cracks where E is the crack arrowed magnification of the crack pointed by the yellow arrow in (d) and (k) line EDS across a typical crack.

crescent keyholes are observed at E≥140 J/mm^3, due to the higher specific laser energy input in agreement with the literature [31]. Lack of fusion, keyholes and cracks defects are illustrated in Fig.5g-E, respectively. The keyhole porosity area fraction decreases with increasing E (see Fig. S5), which agrees with [32], in contrast of the cracks which exist in all samples at E≥140 J/mm^3. Keyholing occurs due to the elemental evaporation from the melting pool during the LPBF process due to the higher E, creating pores [33] and interrupting the nominal chemical composition within the build [34]. This change in elemental chemical composition, due to evaporation, is common and was verified by the chemical analysis of the AF block sample built with E=183J/mm^3 as presented in Table 1.It is worth mentioning that the observed spots in Fig.5f and at samples with high E, are corrosion pits when the samples encountered moisture during polishing. The area of the pits was not considered in any calculations (See optical micrographs in Fig.S6). Typical micro-cracks with an average thickness of 4µm are observed growing longitudinally in parallel with the BD. They occur due to the higher cooling rate and the residual stresses in the LPBF process [35], over and above the inherent brittleness of this alloy, where the inner edges of some of these cracks were pulled out, occasionally during the polishing process and appeared as in Fig5.j. Cracks are occasionally associated with a chemical inhomogeneity surrounding them,

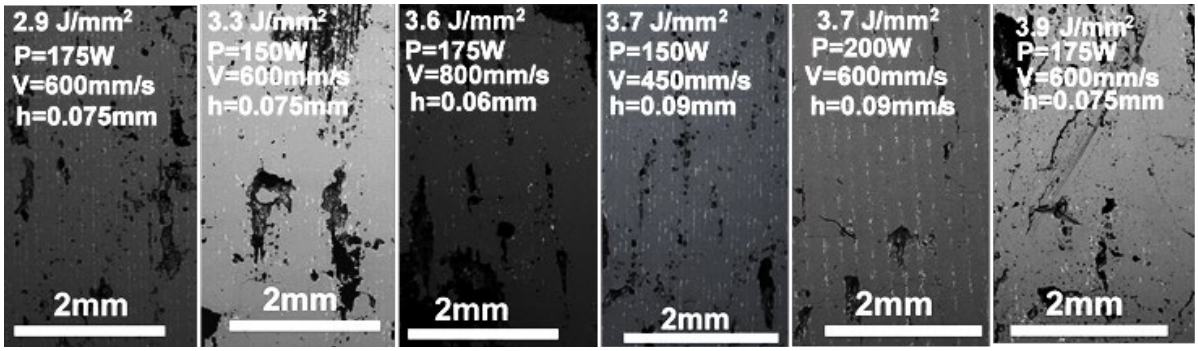

Fig.6: SEM micrographs of the refined microstructure of block samples within 97≤ E≤140J/mm^3.

as seen by the EDS line analysis in Fig.5k. The presence of multiple cracks in some samples revealing the influence of cracking mechanisms by the process parameters. Cracks and pores are also observed in the cast alloy due to the large viscosity of the molten alloy during casting [14]. The AF LPBF samples show segregations of La/Ce rich phases (white segregation), which have been identified as LaCeFeSiO oxide (see Fig.S7). This oxide was reported previously in LPBF processed La-Fe-Co-Si and cast La-Fe-Si alloys, and the oxidation was suggested to occur during the melting/solidification processes and during sample preparation [6,11]. The segregation of La/Ce secondary phases also act as an additional cause for cracking initiation, where it has been reported that La/Ce secondary phases increase cracking susceptibility and propagation along the grain boundaries and through the grains [36], weakening the material's strength and interrupting the elemental chemical composition [35]. It was reported that the crack propagation is stopped once it approaches α-Fe rich phases, due to the dissipation of propagation energy into the α-Fe grain, which is plastically deformed [36].

As predicted by the model, the microstructure of the block samples built with E=293J/mm^3 in Fig.5f, shows the lowest porosity fraction, however, the cracking and chemical composition disturbance cannot be avoided, which will result in undesirable mechanical and magnetic properties. So, the results by the model cannot be applied to this material as the magnetic materials are sensitive to the chemical composition and the volume of non-magnetic secondary phases. Alternatively, a crack-free sample with the lowest porosity should be the next option for an optimised microstructure. The samples built with E=123J/mm^3 is virtually crack-free with the lowest porosity and E=140 J/mm^3, representing a cracking threshold. This means that a new DOE was performed for the blocks within the window processing parameters of 97≤ E≤140J/mm^3, to get a precise refinement of porosity fraction and cracks and the relevant SEM micrographs are presented in Fig.6. The sample built with E=123J/mm^3 (P=150W, V=450mm/s and h=0.09mm) shows a crack-free microstructure with the lowest porosity

fraction, and this condition is recommended as the experimental optimum condition across the whole range. The fact that a certain condition at E=123 J/mm^3 highlights one of the limitations of the energy density concept, which is the potential inconsistency in build quality for the same E. However, it is worth mentioning that the recommended condition (E=123J/mm^3) was built three times to ensure the repeatability in Archmedias density value that shows 6.82 ± 0.21 g/cm^3, 7.01 ± 0.46 g/cm^3 and 6.79 ± 0.15 g/cm^3, respectively.

3.1.3 Lattice struts and MC blocks

The lattice samples show a similar densification mechanism to the block samples, whereby the increase in E improves the build integrity as presented in Fig.7a-d. However, the material remains very brittle and the lattice holes are either clogged, cracked or connected, which explains the higher scatter in Archimedes density data in Fig.3a due to the liquid flow within the pores during the density measurements. Mechanically, lattice strength arises from several factors such as unit cell topology, strut dimensions and bulk mechanical properties [37]. This means, the failure/brittleness of the manufactured lattices can be attributed to the inherent brittleness of the LaCe(Fe,Si,Mn)$_{13}$ raw material [1], the small unit cell size and strut dimensions, which allows for the bending-dominant structure [38]. The MC blocks show the same microstructural behaviour of the block samples, and the SEM micrographs in Fig.7e-h show the influence of E on MC clogging, where the MCs start clogging and distorting at E=140J/mm^3. The MC block samples show a rougher surface and partially melted particles at the inner edges (see Fig.7i-k), which agrees with the previously published results in LPBF MC Ti blocks [39]. However, the diameter of the MC was built fairly precisely, where the difference between the target and the effective diameters ≈10µm (See Fig.7l), the effective diameters were determined using Image J software.

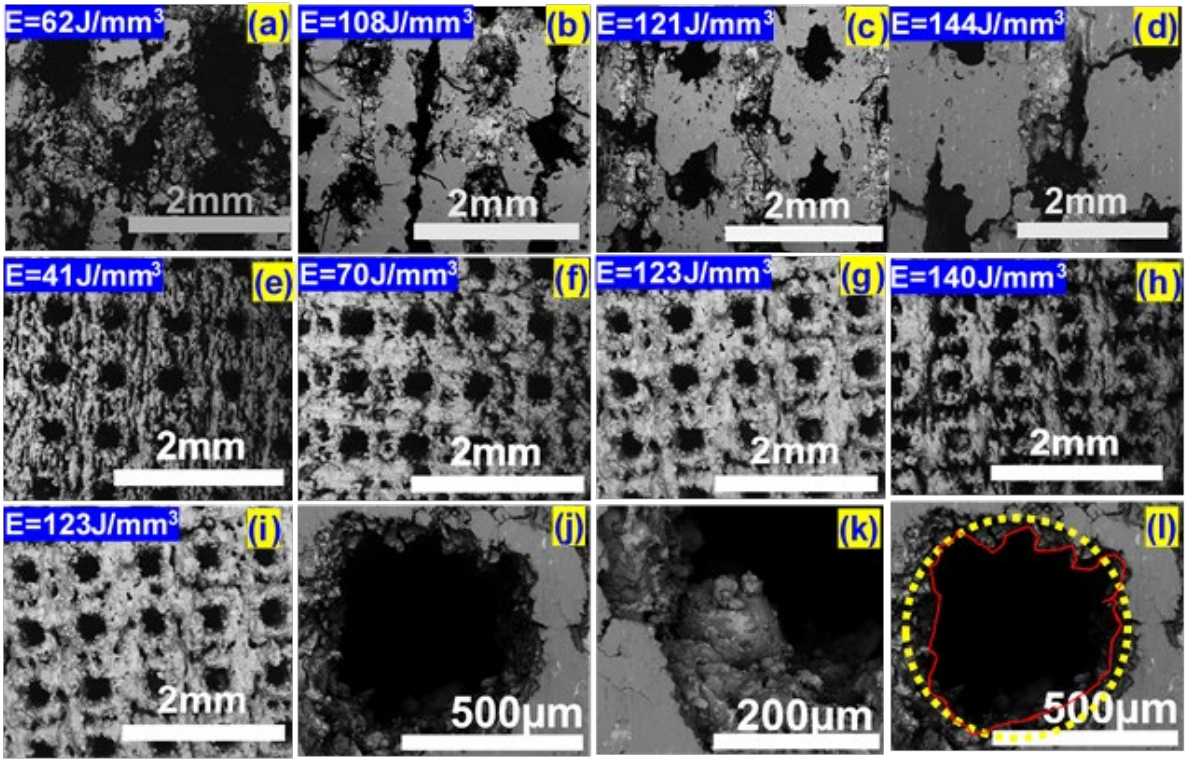

Fig.7: Representative SEM micrographs showing the influence of E on the build integrity of (a,b,c,d) the lattice strut samples, and (e,f,g,h) MC block samples, and (i,j,k,l) the MC sample built with E=123J/mm^3, where, (i) top view, (j) single MC, (k) unmelted particles within the edge of the MC and (l) comparison between the target and effective MC diameter.

3.1.4 Influence of thermal quenching post process on the $NaZn_{13}$-type phase formation

The XRD pattern of the raw powder in Fig. S8a reveals the characteristic's peak reflections of the $NaZn_{13}$-type cubic structure (Fm3c space group) [10, 40] with an extra small peak that belongs to α-Fe rich phase at $2\theta=52.5^{\circ}$. The polycrystalline $NaZn_{13}$-type structure is decomposed during the LPBF process, and the AF samples are predominantly rich in α-Fe and La/Ce phases (see Fig. S8a) within a block sample [11]. The decomposition of $NaZn_{13}$-type structure during the LPBF process can be interpreted as follows: the $NaZn_{13}$ phase is normally formed via a peritectic interaction during solidification [41], where α-Fe and La/Ce dendrites grow in large numbers from the liquid, during LPBF solidification, and trying to interact in a peritectic reaction [6]. However, the peritectic reaction does not progress to completion due to the rapid cooling rate/solidification [41], leading to the confinement of La/Ce rich phases in the interdendritic regions and so non-interacted separate α-Fe and La/Ce rich phases [42], see Fig.8a,b. Following the homogenisation HT at 1050ºC for 168hrs, the $NaZn_{13}$-type structure is rejuvenated due to dendrites degeneration and reaction diffusion between the α-Fe and La/Ce rich phases [6] (See Fig.8c,d), and subsequently frozen due to the quenching process which is

used to avoid thermal decomposition [6] (also see Fig. S8a). It was reported that traditional synthesis methods of La-Fe-Si alloy, such as casting, results in coarse dendrites with segregation. As such, longer homogenisation HT time is required to allow the formation of $NaZn_{13}$ phase [42]. In contrast, in this work, the LPBF process results in finer dendrites due to the high cooling rate, thus requiring a relatively shorter homogenisation time (168 h) for full homogenisation. This homogenisation HT was reported as the shortest required time for La-Fe-Si based alloys that allows the diffusion between α-Fe and La dendrites, forming the $NaZn_{13}$ phase [6], including in samples processed using LPBF [11]. The XRD patterns of the AQ LPBF blocks, built with different E, are presented in Fig.9, where their analysis has confirmed the $NaZn_{13}$ structure (See Fig.S8b,c) with lattice parameters presented in Table 3 . The secondary α-Fe and La/Ce rich phases are observed in all quenched samples in different ratios and have been identified as α(Fe,Si), CeSi, La_5Si_3 and LaFeSi (as indexed in Fig.9), and the intensity of their XRD peaks increases with increasing E, up to E=123J/mm^3, before it decreases beyond E>123J/mm^3. The XRD analysis also shows the increase in the volume of the $NaZn_{13}$ structure with the increase in E (See Table3). Which is consistent with the SEM observation in Fig.10a-c where the grey colour represents the $NaZn_{13}$-type structure phase and the coarse white Lamellae and spherical dark/black segregations represent the La/Ce and α-Fe rich phases, respectively, as identified by the EDS map in Fig.10e. The change in secondary phases fraction was observed in cast alloys with changing annealing temperatures [6,43]. The $NaZn_{13}$ matrix is rich in Si at E≤140J/mm^3, as indicated by the EDS in Fig.S9, due to the depletion of α-Fe and La/Ce because of the higher segregated fractions [6], which suppresses the relevant magnetic properties. The higher E values at E>140J/mm^3 improves the homogeneity and the incorporation of α-Fe and La/Ce in the $NaZn_{13}$ matrix. However, the nominal chemical composition of the alloy is interrupted, see Table 1, due to evaporation.

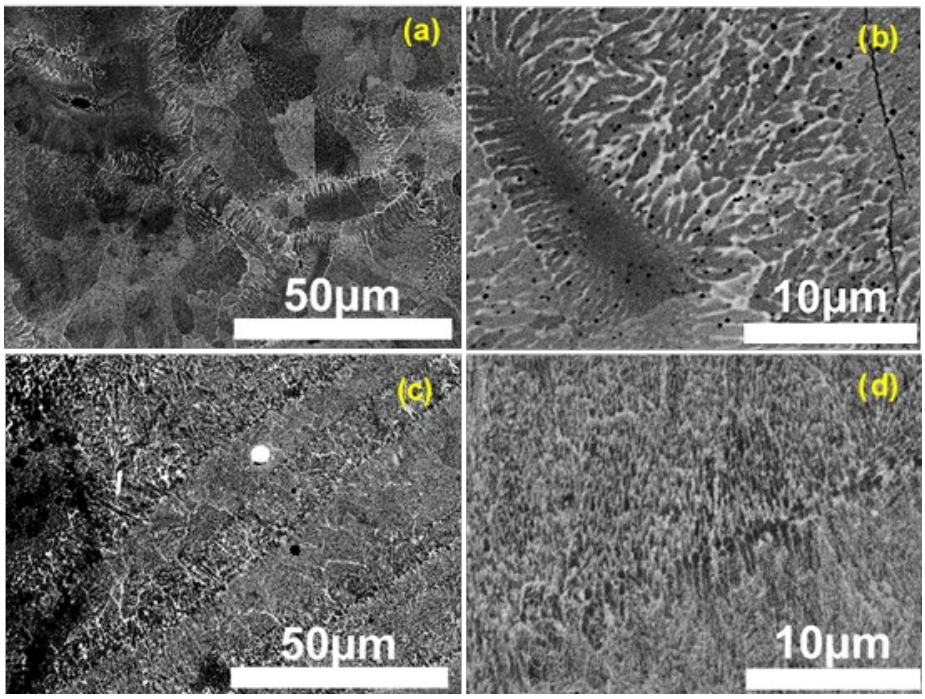

Fig.8: SEM micrographs for the sample LPBF E=140J/mm^3 showing (a,b) the dendritic structure in the AF condition and (c,d) the reaction diffusion after thermal HT homogenisation and quenching.

It is worth mentioning that the formation of α-Fe and La/Ce secondary phases with the $NaZn_{13}$ matrix is in agreement with $La(Fe,Si)_{13}$ phase diagram [44, 45], and have been observed previously in LPBF processed [11] and conventional processed cast [6], arc-melted [10], spark plasma sintered [10] La-Fe-Si alloys. Moreover, it is observed that there is a difference between the shape of the La/Ce and α-Fe secondary phases in the conventional and LPBF processed alloy before and after the thermal HT quenching process. Before quenching, the secondary phases in the current LPBF processed alloy are mostly formed in big particles in well-arranged lines parallel to the build direction (See Fig.5c,d), meanwhile in cast alloy, they are formed in finer pronounced dendritic structure [6]. However, after quenching, the secondary phases degenerate into fine particles in cast alloy and into coarser Lamellae and spherical particles in LPBF alloy similar to the observed in arc-melted alloy [46].

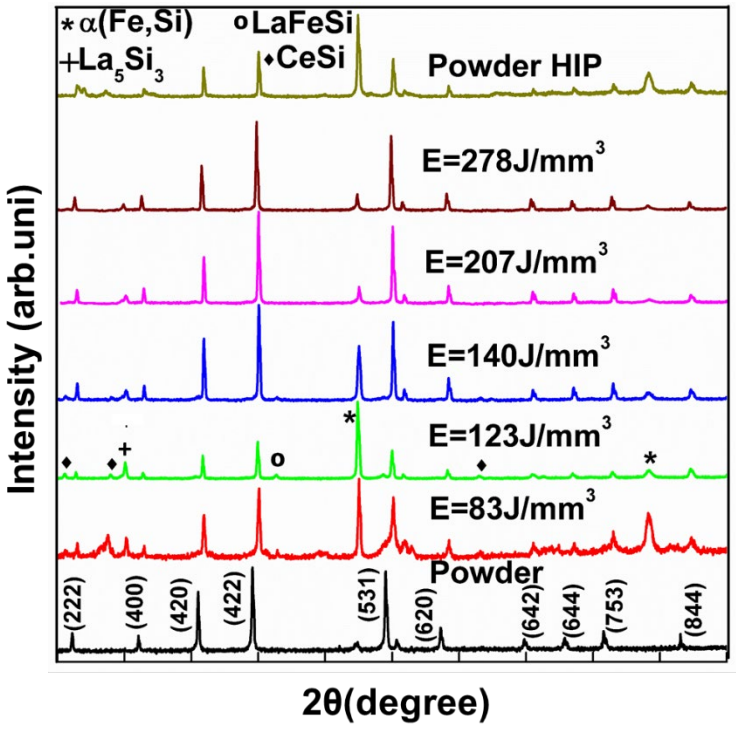

Fig.9: XRD patterns of the as quenched samples built with different E and powder HIP.

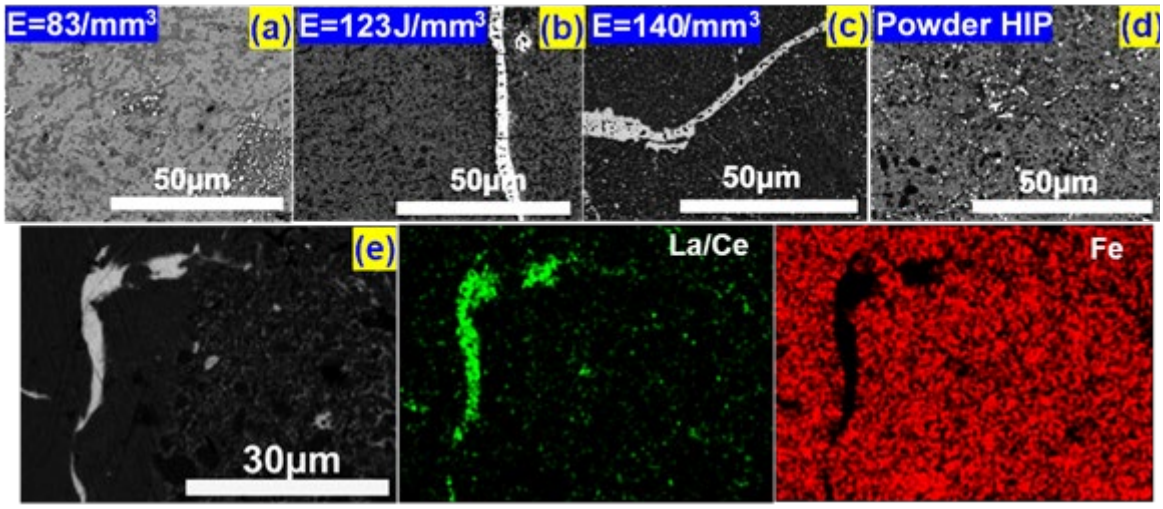

Fig.10: SEM micrographs showing the influence of processing parameters on the fraction of α-Fe and La/Ce rich phases, (a,b,c) As quenched LPBF for block samples built with the titled E, (d) for the powder HIP sample, and (e) EDS map for the secondary phases in LPBF sample .

3.1.5 Influence of powder HIP

The powder HIPed sample shows a dense microstructure, in comparison with the LPBF samples as presented in Fig.10d. HIP effectively collapsed the powder particles under the effect of a simultaneous application of higher pressure and temperature [47]. Finer grains, larger volume of α-Fe and La/Ce secondary phases and lower volume of $NaZn_{13}$ phase are

pronounced at the grain boundaries more than the LPBF samples (see Table 3), which agrees with [48]. In addition, all XRD peak intensities of the HIP sample are lower than the raw powder, which may be due to randomised texture orientation, which characterises the HIP process [48], in contrast with the LPBF samples [26]. In addition, the HIP sample shows a higher promotion in α-Fe phase, meaning that a reduction in the $NaZn_{13}$ phase amount (see Table 3).

3.1.6 Influence of post-LPBF hydrogenation on the $NaZn_{13}$-type structure

The AQ LPBF blocks, MC blocks and powder HIP samples were exposed to extra HT in hydrogen atmosphere at 400°C (hydrogenation process). In this treatment, hydrogen atoms incorporate into $LaCe(Fe,Si,Mn)_{13}$ ($NaZn_{13}$ matrix) interstitially [12], increasing the unit cell volume that appear as a shift of peaks positions towards lower angles (see Fig.S8a, and Table 3), which improves the magnetic properties and shifts the T_c value of the AQ samples towards higher temperatures. Moreover, hydrogen HT has the advantage of decreasing oxides volume that may exist in the AQ samples, improving the magnetic properties (see Table 1) [49]. It is worth mentioning that such HT temperature is low to change the $NaZn_{13}$-type crystal structure of the AQ samples [9,11,40].

3.2 Mechanical properties

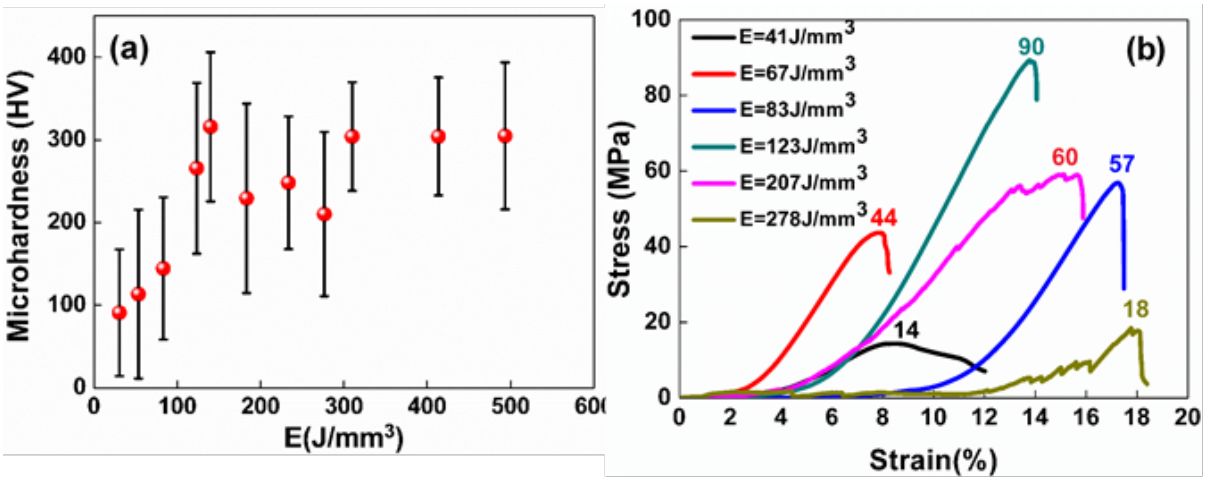

Fig.11: (a) Influence of E on mechanical properties of the HQ samples (a) the average microhardness Vickers (HV) and (b) compressive stress-strain curves for the HQ block samples.

The mechanical strength of a material is affected by its microstructural defects, such as porosity and cracks, as well as the distribution of the various phases that contribute to the strength of this alloy. Strength is an important property, as it indicates the degree of integrity in the build and its likely longevity in an application. The hardness Vickers (HV) data of the

AQ LPBF block samples show higher scattering as seen in Fig.11a since the overall hardness depends on the three phases each with different inherent strength, where the HV of the main $NaZn_{13}$ matrix > La/Ce rich phases > α-Fe rich phases [36]. This means the microhardness data may not give clear microstructure-strength correlations. However, the average HV values show a trend of promotion with the increase E, with a minimum value of 90HV at the lowest E value ($E=31J/mm^3$), passing through an average onset of 275HV at $E=123J/mm^3$ to a maximum value of 305HV at $E=493J/mm^3$. This behaviour is similar behaviour to the LPBF processed Fe-Ni-Si alloys [50], and may be refer to the improvement in the build density and the increase in volume fraction of $NaZn_{13}$ magnetic phase (See Table 3) [51].

Fig.11b shows the compressive stress-strain curves of the HQ LPBF samples. The maximum compressive strength (σ_{max}) increases with increasing E, achieving a maximum value of 90MPa at the sample built with $E=123J/mm^3$, then decreases at higher E. The higher σ_{max} in La-Fe-Si alloys is associated with lower microstructural defects, the presence of α-Fe segregation and the volume of the $NaZn_{13}$ phase. Where the microstructural defects (cracks and porosity) result in spaces within the bulk material, leading to lower mechanical strength [52]. In addition, it was reported that the presence of α-Fe segregation in La-Fe-Si alloys increases their mechanical strength [16,53]. These explain the monotonic increase in σ_{max} below $E=123J/mm^3$, which is due to the lower porosity and presence of α-Fe segregated in these samples. Meanwhile, the lower σ_{max} beyond $E=123J/mm^3$ refers to lower α-Fe and the presence of cracks, which is the main source of the weak mechanical strength. It is worth mentioning that σ_{max} value of the sample $E=123J/mm^3$ (the optimised condition) is higher than the reported value for the arc-melted $LaFe_{11}Si_{1.4}$ (63MPa) [52] and lower than arc-melted $LaFe_{11.7}Si_{1.3}C_{0.2}$ (120MPa) [54].

3.3 Magnetic properties

3.3.1 Temperature dependence of magnetisation

The temperature dependence of the direct current (dc) magnetisation curves (M(T)) of the raw powder, AF, AQ and HQ LPBF, MC block and powder HIP samples are presented in Fig.12. The M(T) curve of the pre-alloyed powder in Fig.12a shows a two-stage magnetic transition: a sluggish ferromagnetic spin glass transition near 150K followed by a sharp IEM FM-PM transition at the Curie temperature (T_c) of 295K. The T_c value corresponds to the minimum of the dM/dT curve, as illustrated in the inset of Fig.12a. The FM-PM transition occurs due to the exchange interaction between the Fe-Fe and La-Fe bonds [6,9]. The FM

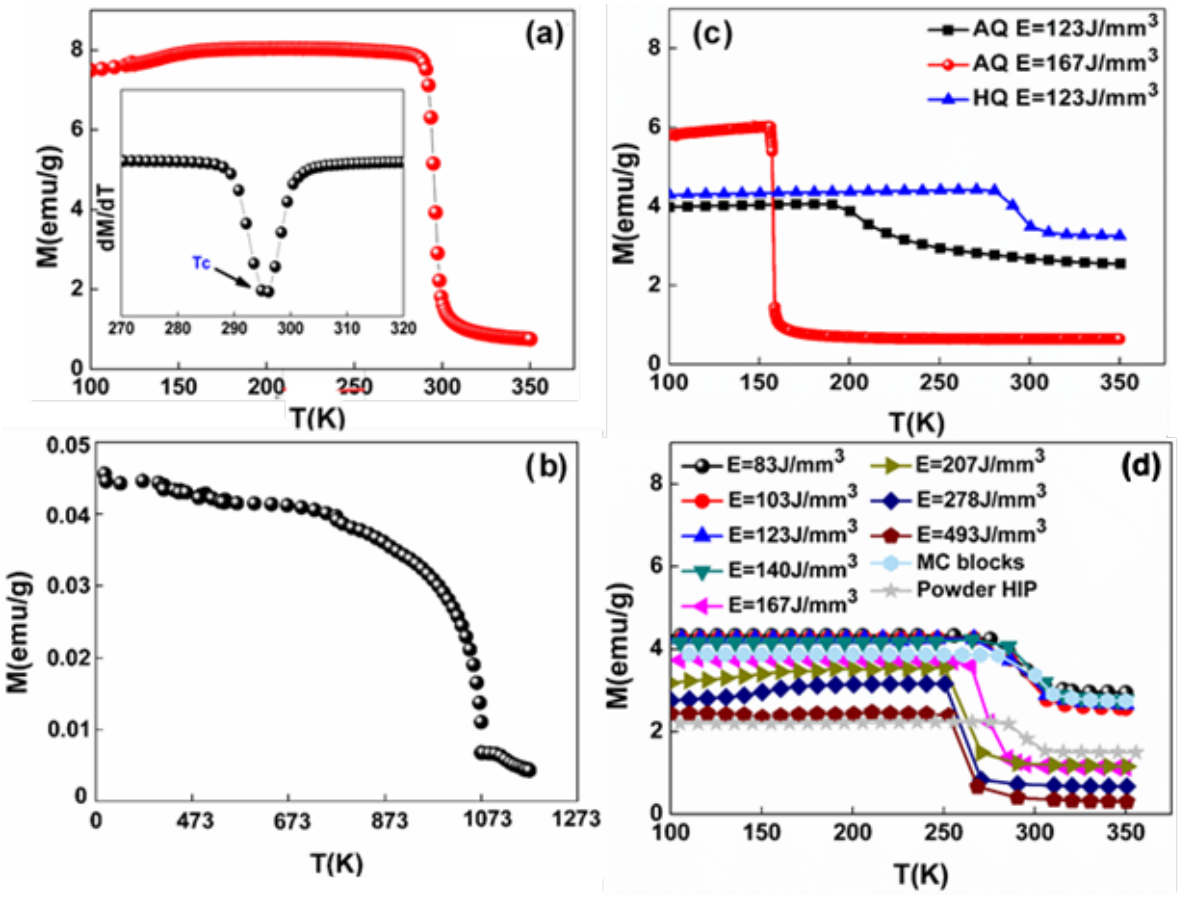

Fig.12: Temperature dependence of magnetisation curves of (a) raw powder sample and the dM/dT in the inset, (b) AF LPBF block sample built with E=123J/mm^3, (c) AQ, HQ LPBF block sample built with E=123J/mm^3, AQ LPBF block sample built with E=167J/mm^3, and (d) all HQ LPBF block samples, MC block and HIP powder samples.

environment is interrupted by the presence of Mn atoms which creates antiferromagnetic (AFM) coupling with Fe, diluting the FM ordering and leading to the FM spin glass transition at 150K [55]. The $NaZn_{13}$ matrix relevant T_c disappears in the AF LPBF samples and the magnetisation is suppressed due to the decomposition of the magnetic matrix during the LPBF process, as confirmed by the XRD (Fig. S8a). Instead, they only show a high temperature T_c at 1043K, as seen in Fig.12b, which belongs to the predominant α-Fe phase [56].

Due to the homogenisation of the $NaZn_{13}$ matrix after the thermal quenching, the magnetisation increases again and the AQ LPBF samples built with E≤140J/mm^3 (including the MC block sample) show a constant T_c value of 210K, as seen in Fig.12c for the sample E=123J/mm^3, which is the typical IEM FM-PM transition temperature of this alloy [6,10]. Meanwhile, the T_c value of the AQ LPBF samples built with E>140 J/mm^3 decreases to 158K (see Fig. 12c) for the sample at E=167J/mm^3. The Fe-Fe interatomic distance plays an

important role in controlling the electronic exchange and so the T_c, where the Fe-Fe FM coupling occurs only when the interatomic distance of Fe-Fe ≥2.45Å [43]. This raises the possibility of controlling the T_c by increasing the Fe-Fe interatomic distance via interstitial atoms [12]. The hydrogenation process allows for the incorporation of hydrogen as interstitial atoms with the $NaZn_{13}$ matrix. This improves the magnetic properties of the AQ LPBF and powder HIP samples without changing the crystal structure (See Fig.S8a), where it causes a drastic shift in the T_c towards room temperature and increases the magnetisation [40] (see HQ sample in Fig.12c). The significant enhancement in the T_c, and the magnetisation of the HQ samples, is attributed to the expansion of the lattice constants' caused by the interstitial hydrogen atoms [57] (See Table 3) and the oxygen reduction due to hydrogen heat treatment (See Table 1) [49]. The lattice constants expansion reduces the bandwidth of the 3d orbital of Fe atoms, which decreases the overlap between their electron wave functions [58]. This, simultaneously, improves the electronic exchange between the short Fe-Fe bonds, allowing for the promotion in the T_c [59]. Fujita *et al.* have reported impossible electronic exchanges between hydrogen and Fe atoms in $La(Fe,Si)_{13}H_y$ [60], which confirms the unit cell volume expansion is the dominant mechanism for the magnetic coupling. The HQ LPBF block samples, built with E≤140J/mm^3, the MC block and the powder HIPed in Fig.12d show a sluggish T_c around 290K with freedom of +4K for some samples (the change is around T_c≈95K from the AQ samples) due to the high fraction of secondary phases [61]. Meanwhile, the HQ LPBF block samples built with E>140J/mm^3 show a sharp T_c around 260K. The samples do not show a large thermal hysteresis, where the maximum registered thermal hysteresis is 4K (see Fig.S10). The DSC measurements in Fig.13 confirms the phase transition temperatures of the HQ block samples, with some having freedom of ±4K. The big difference in magnetisation and T_c values between the AQ LPBF block samples and the pre-alloyed powder refers to the hydrogen rich content in the pre-alloyed powder, which is evaporated during the LPBF process. It is worth mentioning that T_c is an intrinsic property that depends on the ferromagnetism inside the grain and is governed by the electronic exchange between Fe-Fe atoms [62,63]. This means, the T_c may be not affected by the extrinsic defects, instead influenced more by the elemental chemical composition, especially Si in $La(Fe,Si)_{13}$ alloys [63], where it was reported that a 20% decrease of Si content in $La(Fe,Si)_{13}$ alloy decreases the T_c value by 12K [64]. The T_c dependence on E was reported previously in the AF LPBF Mn-Fe-P-Si magnetocaloric alloy and has been attributed to the change in lattice parameters with E as a result of the induced residual stresses at higher E [65]. However, in this study, the extended homogenisation HT process, which was applied on the AF samples likely relieved almost all of residual stresses

[26], excluding any significant changes in the lattice parameters and so the T_c. Accordingly, the constant T_c value in the AQ LPBF samples built with E≤140 J/mm^3 likely occurs due to the close chemical composition and the electronic exchange inside the grain of the $NaZn_{13}$ magnetic matrix, which is preserved without any influence by grain boundaries or defects [62, 63]. However, the decrease of the T_c at the AQ LPBF blocks built with E>140 J/mm^3 may occur as a result of the disturbance in the elemental chemical composition of the $NaZn_{13}$ matrix by evaporation during the LPBF process at higher E, which is confirmed by the chemical analysis of the block sample with higher E (E=183J/mm^3) in Table 1. Despite of the decrease in Mn ratio by evaporation, which should promote the FM properties via decreasing the AFM Mn-Fe coupling, the decrease in Si is more effective. The AQ LPBF MC block and the AQ powder HIP samples show the same T_c value of the AQ LPBF samples built with E≤140J/mm^3 and the M(T) curves are presented Fig.12d, however, the magnetisation of the HIP powder sample is lower.

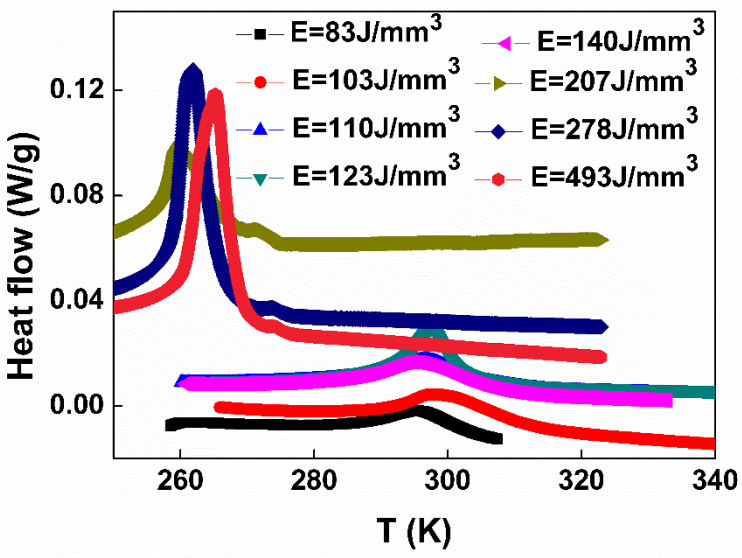

Fig.13: DSC measurements of the HQ LPBF block samples.

3.3.2 Isothermal magnetisation

Fig.14a-c shows the M(H) curves of the powder and the HQ LPBF samples built with E=123J/mm^3 and E=493J/mm^3, respectively. In each, the saturation magnetisation decreases monotonically with the elevating of the temperature, due to the spin disorder. The IEM FM-PM transition is asserted in the M(H) measurements, where the magnetisation in all curves below the T_c increases sharply with the increase in $\mu_0 H$ and saturates at ≈0.5T as a character of

the FM behaviour, before changing linearly with the magnetic field above the T_c in correspondence with the PM behaviour. The nature of the FM-PM transition (first or second order) has a strong impact on the MCE properties, where the first order phase transition (FOPT) is accompanied by higher MCE. So, Arrott plots in Fig.14d-f were induced from the M(H) curves and employed to determine the FM-PM transition type. The negative slope and the S-shape of Arrott plots around the T_c characterise the FOPT, meanwhile, the positive slope reveals the second order phase transition (SOPT) [66]. According to these criteria, the raw powder in Fig.14d and the HQ LPBF block samples built with E>140J/mm^3 in Fig. 14f show FOPT IEM transition that is echoed by the negative slope and S-shape of Arrott plots around the T_c as illustrated by the arrows. Meanwhile, the HQ LPBF block samples built with E≤140J/mm^3 show the SOPT due to the positive slope of Arrott plots around T_c (See Fig.14e), which is also the case of the MC block and the powder HIP samples. The La(Fe,Si)$_{13}$ based alloys are known with the FOPT [7,10]. However, the observed SOPT at E≤140J/mm^3 was reported previously in LPBF processed La(Fe,Co,Si)$_{13}$ [11] and arc melted LaFeSi alloys [67], and is attributed to the Si rich content in the NaZn$_{13}$ magnetic matrix [5, 68] due to the high depletion of α-Fe, where Si rich La(Fe,Si)$_{13}$ alloys have been reported as SOPT magnetocaloric alloy [60, 67,68]. The SOPT-FOPT crossover at E>140J/mm^3 is attributed to the decrease in the fraction of the secondary phases and their incorporation into the magnetic matrix that increases with E, increasing homogeneity and approaching the nominal composition that could not be reached due to evaporation [68, 69]. The DSC in Fig.13 provide additional confirmation of the crossover of the SOPT-FOPT, where the FOPT is characterised by a sharp peaks of heat flow due to the associated heat latent, which is the case at the sample with E>140J/mm^3, meanwhile, the samples with E≤140J/mm^3 shows the characteristics of SOPT as they show lambda-like cusp in the heat flow in agreement with [67].

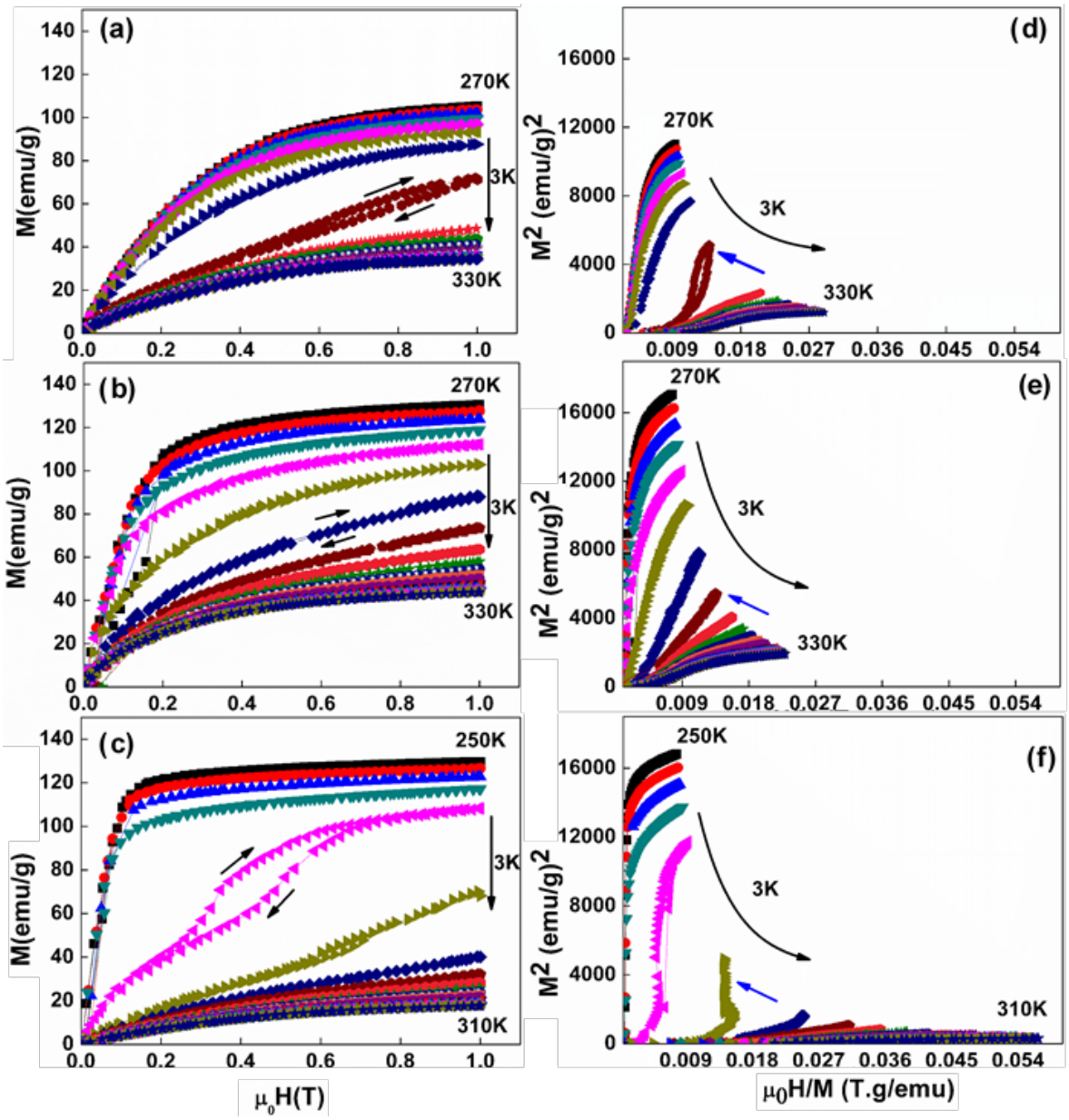

Fig.14: (a,b,c) Isothermal magnetisation curves of powder, HQ LPBF block sample with E=123J/mm^3 and E=493J/mm^3, (d,e,f) the relevant induced Arrott plots, where different colours represent the change in temperature.

3.3.3 Magnetocaloric effect (MCE)

The MCE performance of the powder and HQ LPBF block samples are presented in Fig.15. As seen in Fig.15a, the temperature dependence of ΔS of the raw powder, ΔS(T), shows a maximum (ΔS_{max}) around the T_c which increases monotonically with the increase in $\mu_0 H$. More ΔS(T,H) curves are available in Fig.S11 for the HQ LPBF block samples. It is worth mentioning that ΔS data also can confirm the nature of magnetic phase transition (FOPT/SOPT) via the ΔS dependence on magnetic field as in equation 3 [70], where **n** is a

constant that is greater than 2 in case of FOPT (E>140J/mm^3) and less than 2 in SPOT (≤140J/mm^3) (See Fig.S12) [67,71]

$$\Delta S \alpha H^n \qquad (3)$$

The raw powder achieves ΔS_{max} value of ≈ 6J/kg.K at $\mu_0 H$=1T. This high value refers to the strong FOPT, which is accompanied by a large abrupt change in lattice constants around the T_c [69]. This value is suppressed in the AQ samples, built with E≤140J/mm^3. For example, the AQ block sample built with E=83J/mm^3, shows ΔS_{max} value of 4J/kg.K at 200K, which is further suppressed to 3.6J/kg.K at 290K in the hydride sample (See Fig.15b), in agreement with [12]. Fig.15c shows ΔS(T) curves for all the HQ LPBF block samples and ΔS_{max} values are listed in Table 3. Where, the maximum achieved room temperature ΔS_{max} values were observed at the block sample built E=123J/mm^3, where it shows 4.9J/kg.K at $\mu_0 H$=1T. The ΔS_{max} values of the HQ LPBF block samples built with E≤140J/mm^3 achieve ≈50-81% of the maximum value in the raw powder. Meanwhile, the HQ LPBF block samples, built with E>140J/mm^3, show higher ΔS_{max} values of 4.3J/kg.K, 6.2J/kg.K and 6.7J/kg.K for E=207J/mm^3, 277J/mm^3 and 493J/mm^3, respectively, around 260K. These higher values represent ≈72%, 103% and 111% of the achieved values by the raw powder, respectively. The higher ΔS values of the block samples than the raw powder was observed previously in the LPBF Mn-Fe-P-Si magnetocaloric alloy and has been attributed to the stronger FOPT in the respective bulk samples as seen in Fig.14c [65].

The ΔS_{max} dependence on E is depicted in Fig.15d, as ΔS_{max} increases monotonically with the increase in E [65]. The ΔS_{max}(E) relation cannot be interpreted according to the improvement in the microstructural defects, as ΔS is an intrinsic property [72], instead, it is more likely related to the influence of E on homogeneity. This concept is confirmed by the reported results of LPBF MnPSi magnetocaloric material, where the MCE increases with cracking as E increases [65].

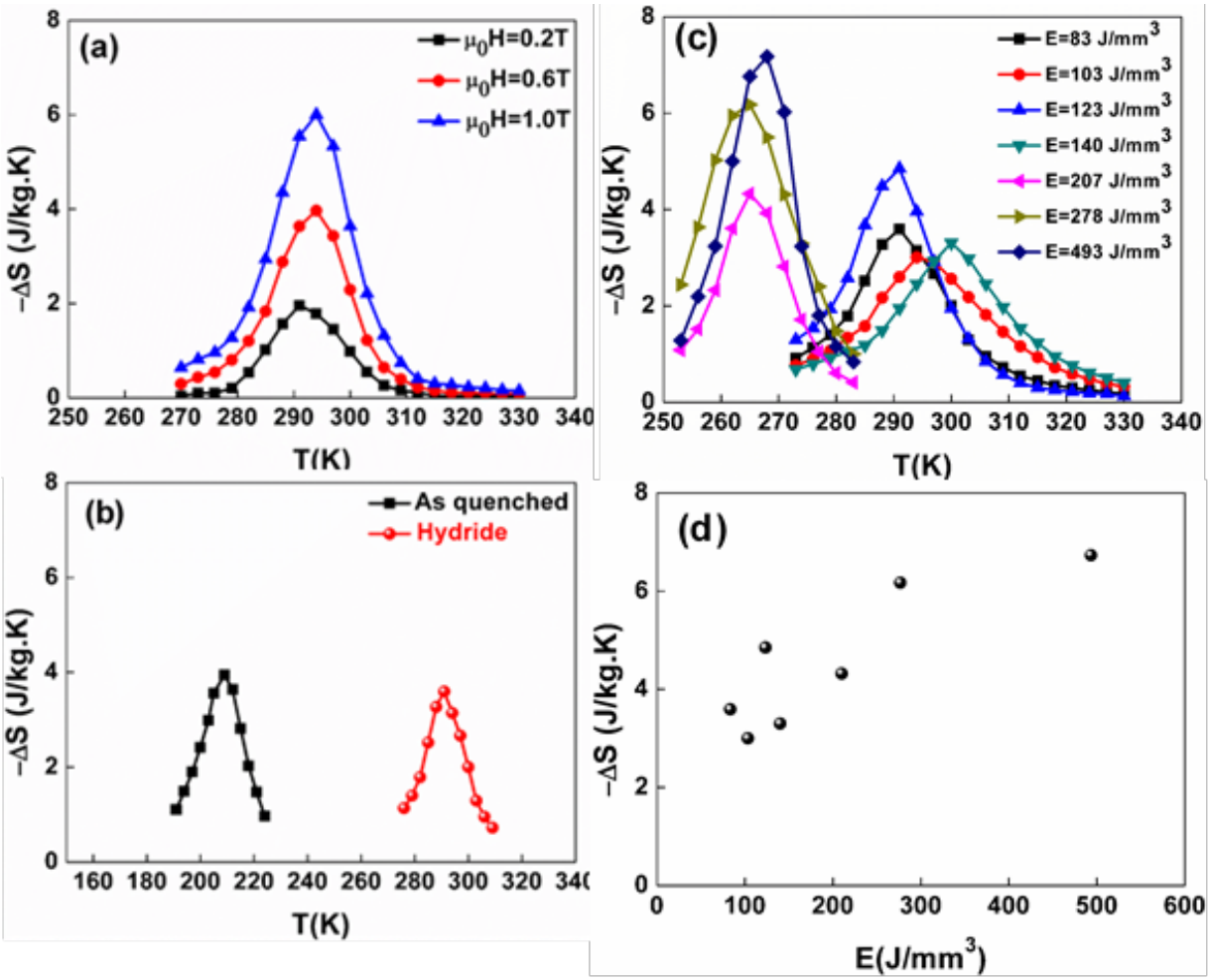

Fig.15: (a) Thermal variation of ΔS at different values of μ_0H for powder, (b) the influence of hydrogenation process on ΔS and T_c for the LPBF block sample built with E=83J/mm^3, (c) ΔS(T) curves of the HQ LPBF block samples built with different E at μ_0H=1T and (d) ΔS dependence on E.

The segregation of La/Ce and α-Fe secondary phases decreases the volume of the magnetic $NaZn_{13}$ matrix, which is being depleted from crucial elements. Despite of the played role of α-Fe in the mechanical stability in the currently processed alloy, but the segregated α-Fe volume suppresses the magnetic and magnetocaloric properties [16]. Therefore, the observed high α-Fe precipitation at E≤140J/mm^2 decreases ΔS_{max} value by two means, first, its soft ferromagnetic nature and the second is the α-Fe depletion from the $NaZn_{13}$ matrix that increases the Si ratio, leading to SOPT and lower ΔS_{max} values [5,68]. Therefore, the low segregated α-Fe volume at higher E (E>140J/mm^3) (See XRD) suggesting its incorporation into the $NaZn_{13}$ magnetic matrix, preserving the nominal Si value and the FOPT of the magnetic matrix [66, 68] and so leading to higher ΔS. However, ΔS values could be improved even by adding more percentages of the evaporated elements or could be by using other additive manufacturing technique whose operation does not require application of higher temperature than the melting temperature of the processed alloy (1450°C) such as binder jetting.

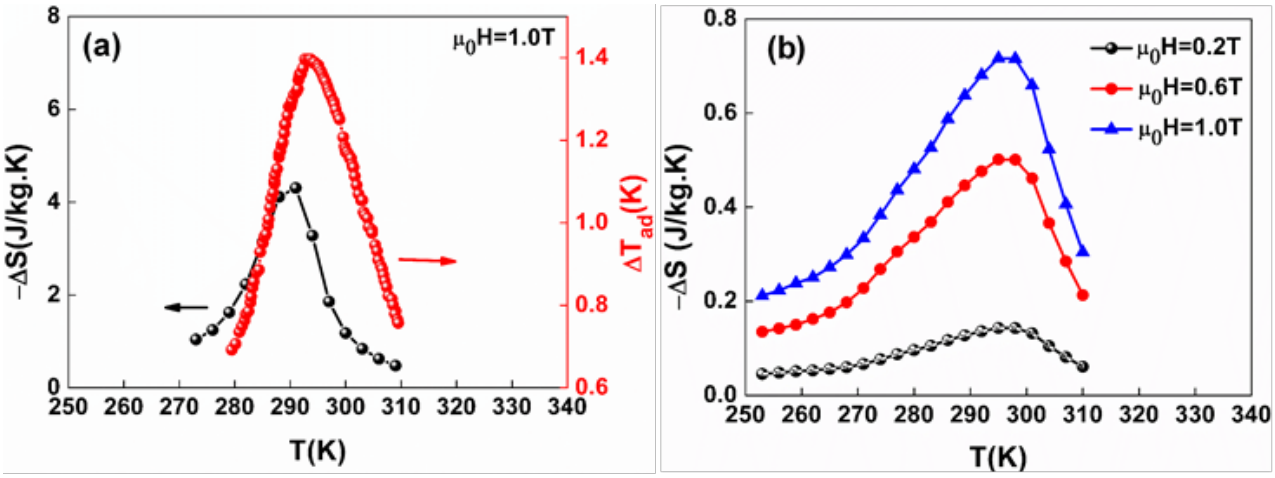

Fig.16: Thermal variation of ΔS and ΔT_{ad} of the HQ MC block sample built with E=123J/mm^3 and (b) the thermal variation of powder HIP sample under the effect of different values of μ_0H.

As seen in Fig.16a, the HQ MC block sample, built with E=123J/mm^3, shows a close ΔS_{max} value (4.2J/kg.K) to the block sample built with the same E condition, revealing the consistency in the MCE results. In addition, the MC block sample shows a maximum adiabatic temperature change (ΔT_{ad}) of 1.41K at μ_0H=1T, which is close to the LPBF La(Fe,Co,Si)$_{13}$ alloy (ΔT_{ad}=1.51K, μ_0H=1.9T) [11] and 50% of the value achieved by sintering method [73]. Fig. 16b shows the powder HIP sample does not show promising MCE properties, where it shows a ΔS_{max} value of 0.72J/kg.K at μ_0H=1T, which is 14% of the achieved value by the HQ LPBF block samples at room temperature. This smaller ΔS_{max} value refers to the SOPT and the lower fraction of the $NaZn_{13}$ magnetic matrix (See Table 3) due to the excess/fine segregation of Fe and La/Ce rich phases, which are known to damp the MCE properties [6]. The MCE properties of the lattice strut samples have not been considered due to the fragility and the brittleness, which would acquire them much degradability during the refrigeration cycle.

Table3: Lattice parameter (a) of the AQ and HQ samples, fraction of $Nazn_{13}$ in the AQ samples and comparison between the MCE properties of the current study with other La-Fe-Si based systems synthesised with different methods.

Material	a(Å) AQ	a(Å) HQ	$NaZn_{13}$ wt(%)	Tc (K)	μ_0H (T)	Synthesis method	ΔS_m (J/kg.K)	ΔT_{ad} (K)	Ref
E=83J/mm^3	11.452	11.511	63	295	1	LPBF	3.59		This work
E=103J/mm^3	-	-	-	290	1	LPBF	3		This work
E=123J/mm^3	11.464	11.536	68	290	1	LPBF	4.9		This work
E=140J/mm^3	11.451	11.569	74	290	1	LPBF	3.3		This work
E=207J/mm^3	11.486	11.59	85	290	1	LPBF	4.3		This work
E=278J/mm^3	11.496	11.599	84	260	1	LPBF	6.2		This work
E=493J/mm^3	-	-	-	260	1	LPBF	7.2		This work
Powder HIP	11.466	-	66	290	1	HIP	0.72		This work
Pure Gd				294	2		4.5	-	[2]
$LaFe_{13.92}Si_{1.4}$				194	1	cast	4	-	[14]
$LaFe_{11.6}Si_{1.4}$				225	1	Plasma sintering	1.8	-	[10]
$LaFe_{10.7}Co_{1.3}Si$				325	1.9	LPBF	3.1	1.51	[11]
$LaFe_{11.3}Co_{0.4}Si_{1.3}$				255	2	Induction	5	-	[62]
$La_{0.6}Ce_{0.4}Fe_{11}Si_2H_y$				317	1	arc melted	10	-	[63]
$La_{0.8}Ce_{0.2}Fe_{12.5}Mn_{0.2}Si_{1.3}H_y$				298	1	arc melted	6	-	[64]
$La_{0.7}Ce_{0.3}Fe_{11.4}Si_{1.56}$				195	1	arc melted	19	-	[8]
$LaFe_{11.3}Co_{0.4}Si_{1.3}$				320	1	Sintered	-	3	[65]

Table 3 shows a comparison in the MCE performance of our LPBF samples and other La-Fe-Si based alloys. The results are somewhat promising and show a possible application of the 3D printed $LaCe(Fe,Mn,Si)_{13}$ alloy built with E<140J/mm^3 in magnetic refrigeration technology at room temperature, in particular, the 3D printed MC block prototype that compromises the MCE performance of the bulk alloy with larger surface areas of the porous geometry and mechanical integrity. This decreases the time of heat exchange from the MCE material to the fluid, increasing the refrigeration efficiency [74] and moving the prototype a step forward in mass production. However, there are still important challenges that need to be addressed such as increasing the room temperature MCE and eliminating the induced cracks. The MCE performance of the samples are still quite low in comparison with almost of conventional synthesis alloy, so extra investigation is needed at higher E considering adding extra La,Ce,Si and Mn to balance the evaporated ratios and recover the superior room

temperature MCE performance. In addition, cracking still represent another challenging problem, due to the possible formation of La/Ce phase-relevant cracks during the magnetocaloric cycle if the difference between the thermal expansion coefficient of the $NaZn_{13}$ magnetic matrix and the La/Ce rich phases is significant [36]. So, it is strongly recommended to conduct the future suggested investigation on top of a pre-heated substrate using a hot powder bed [75]. Lastly, using the Maxwell equation in ΔS calculation of SOPT is applicable; however, many concerns have been raised during its use in FOPT systems due to the higher thermal hysteresis [6]. However, its applicability has been reported in FOPT systems with lower or negligible thermal hysteresis (<0.2T), which is the case in this study [6].

Conclusion

This study investigated the 3D printing of porous structures of $LaCe(Fe,Mn,Si)_{13}$ magnetic refrigerant using the LPBF technique. The laser processing parameters were optimised for optimal dense blocks, lattice strut and MC block structures. The condition of E=123J/mm^3 shows the lowest porosity fraction and crack-free with an average density of 6.8 g/cm^3, which has been recommended as the optimal condition. However, the lattice strut's microstructure was brittle. ΔS of the HQ LPBF blocks increases monotonically with the increase in E due to the increase in homogeneity and because of the incorporation of the secondary phases into the main magnetic matrix. The maximum ΔS_{max} value was achieved by the sample built with E=493J/mm^3 (7.2J/kg.K), however this value is achieved Tc value of 260K that is far away from the room temperature application, which is the target of this work. Alternatively, the maximum room temperature ΔS_{max} value achieved by the sample built with optimum condition E=123J/mm^3 is ΔS_{max} =4.9J/kg.K represents 81% of the value achieved by the raw powder. A similar ΔS_{max} value was achieved by the MC block sample built with the same E condition, revealing the consistency in the MCE properties, with ΔT_{ad} value of 1.4K at $\mu_0 H$=1T. The results show the successful build of MC block of $LaCe(Fe,Mn,Si)_{13}$ magnetic refrigerant with higher MCE efficiency as the same of the block.

Author contributions

AAM fabricated the samples and performed the microstructural and magnetic properties characterisation, assisted by MK and RSS in performing the magnetic properties characterisation. MMA proposed and supervised the project and assisted in the interpretation of the results and the development of the manuscript. All the authors reviewed the manuscript.

Acknowledgements

The authors would like to thank Dr. Alessandro Pastore from Camfridge for the provision of the material, and the useful discussions about this work. The assistance of the undergraduate students Hamesh (Fred) Chanter, Sam Haye, and James Foley are acknowledged.

References

1- M. H. Phan, S.C.Yu, Review of the magnetocaloric effect in manganite materials, J. Magn. Magn. Mater. 308 (2007) 325.

2- V. Chaudhary, X. Chen, R.V. Ramanujan, Iron and manganese based magnetocaloric materials for near room temperature thermal management, Prog. Mater. Sci 100 (2019) 64.

3- V. Franco, J.S. Blázquez, B. Ingale, and A. Conde, The Magnetocaloric Effect and Magnetic Refrigeration Near Room Temperature:Materials and Models, Annu. Rev. Mater. Res. 42 (2012) 305.

4- S. Yu. Dan'kov, A. M. Tishi, V. K. Pecharsky, K. A. Gschneidner, Jr., Magnetic phase transitions and the magnetothermal properties of gadolinium, Phy. Rev. B 57 (1998) 3478.

5- A.T. Saito, T. Kobayashi, H. Tsuji, Magnetocaloric effect of new spherical magnetic refrigerant particlesof $La(Fe_{1-x-y}Co_xSi_y)_{13}$ compounds, J. Magn. Magn. Mater. 310 (2007) 2808

6- J. Liu, M. Krautz, K. Skokov, T. G. Woodcock, O. Gutfleisch, Systematic study of the microstructure, entropy change and adiabatic temperature change in optimized La–Fe–Si alloys, Acta Materialia 59 (2011) 3602.

7- A. Fujita, S. Fujieda, Y. Hasegawa, and K. Fukamichi, Itinerant-electron metamagnetic transition and large magnetocaloric effects in $La(Fe_xSi_{1-x})_{13}$ compounds and their hydrides, Phys. Rev. B 67 (2003) 104416.

8- S. Fujieda, A. Fujita, and K. Fukamichi, N. Hirano, S. Nagaya, Large magnetocaloric effects enhanced by partial substitution of Ce for La in $La(Fe_{0.88}Si_{0.22})_{13}$ compound, J. Alloy Compds. 408 (2006) 1165.

9- F. Wang, Y.F. Chen, G.J.Wang, B.G.Shen, The effect of Mn substitution in $LaFe_{11.7Si1.3}$ compound on the magnetic properties and magnetic entropy changes, J. Phys. D: Appl. Phys. 36 (2003) 1–3

10- P. Shamba, N. A. Morley, O. Cespedes, I. M. Reaney, W. M. Rainforth, Optimization of magnetocaloric properties of arc-melted and spark plasma-sintered $LaFe_{11.6}Si_{1.4}$, Appl. Phys. A 122 (2016) 732.

11- J. D. Moore, D. Klemm, D. Lindackers, S. Grasemann, R. Träger, J. Eckert, L. Löber, S. Scudino, M. Katter, A. Barcza, K. P. Skokov, and O. Gutfleisch, Selective laser melting of La(Fe,Co,Si)$_{13}$ geometries for magnetic refrigeration, J. Appl. Phys. 114 (2013) 043907.

12- Y. F. Chen, F. Wang, B. G. Shen . G.j. Wang, J. Sun, Magnetism and magnetic entropy change of $LaFe_{11.6}Si_{1.4}C_x$ (x = 0-0.6) interstitial compounds. J Appl Phys, 93 (2003) 1323.

13- F.X. Hu, B.G. Shen, J.R. Sun, G. J Wang, Z.H. Cheng, Very large magnetic entropy change near room temperature in $LaFe_{11.2}Co_{0.7}Si_{1.1}$, Appl. Phys. Lett. 80 (2002)826.

14- Y. Ouyang, M. Zhang, A. Yan, W. Wang, F. Guillou, J. Liu, Plastically deformed La_Fe_Si: Microstructural evolution, magnetocaloric effect and anisotropic thermal conductivity, Acta Materialia 187 (2020) 1.

15- H. Zhang, Y. Sun, Y. Li, Y. Wu, Y. Long, J. Shen, F. Hu, J. Sun, B. Shen, Mechanical properties and magnetocaloric effects in La(Fe,Si)$_{13}$ hydrides bonded with different epoxy resins, J. Appl. Phys. 117 (2015) 063902.

16- Y. Shao, J. Liu, M. Zhang , A. Yan, K. P. Skokov, D. Y. Karpenkov, O. Gutfleisch, High-performance solid-state cooling materials: Balancing magnetocaloric and non-magnetic properties in dual phase La-Fe-Si, Acta Materialia 125 (2017) 506.

17- C.V. Mikler , V. Chaudhary, T. Borkar, V. Soni, D. Choudhuri, R.V. Ramanujan, R. Banerjee, Laser additive processing of Ni-Fe-V and Ni-Fe-Mo Permalloys: Microstructure and magnetic properties, Materials Letters 192 (2017) 9–11

18- M.S.K.K.Y. Nartu, A. Jagetia, V. Chaudhary, S.A. Mantri, E. Ivanov , N.B. Dahotre, R.V. Ramanujan, R. Banerjee, Magnetic and mechanical properties of an additively manufactured equiatomic CoFeNi complex concentrated alloy, Scripta Materialia 187 (2020) 30–36.

19- C. Shen, K. D. Liss, M. Reid, Z.Pan, X. Hua, F. Li, G. Mou, Y. Huang, Y. Zhua, H. Li, Fabrication of FeNi intermetallic using the wire-arc additive manufacturing process: A feasibility and neutron diffraction phase characterization study, J. Manufacturing processes, 57 (2020) 691

20- H.Tiismus, A. Kallaste, A. Belahcen, M. Tarraste, T. Vaimann, A. Rassõlkin , B. Asad, and P. S. Ghahfarokhi, AC Magnetic Loss Reduction of SLM Processed Fe-Si for Additive Manufacturing of Electrical Machines, Energies, 14 (**2021)** 1241

21- V. Chaudhary, N.M. S.K. K. Yadav, S. A. Mantri, S.Dasari, A. Jagetia, R.V. Ramanujan, R. Banerjee, Additive manufacturing of functionally graded CoeFe and NieFe magnetic materials, J. Alloy Compds 823 (2020) 153817.

22- F. Bittner · J. Thielsch · W. G. Drossel, Laser powder bed fusion of Nd–Fe–B permanent magnets, Progress in Additive Manufacturing 5 (2020):3–9.

23- V. Chaudhary, S.A. Mantri, R.V. Ramanujan, R. Banerjee, Additive manufacturing of magnetic materials, Progress in Materials Science 114 (2020) 100688.

24- Standard Test Methods for Density of Compacted or Sintered Powder Metallurgy(PM) Products Using Archimedes' Principle, ASTM B962 e 17.

25- L.N. Carter, X. Wang, N. Read, R. Khan, M. Aristizabal, K. Essa, M.M. Attallah, Process optimisation of selective laser melting using energy density model for nickel based superalloys, Mater. Sci. Techn. 32 (2015) 657.

26- A.A Mohamed, J. Zou, R S. Sheridan, K. Bong, M. M. Attallah, Magnetic shielding promotion via the control of magnetic anisotropy and thermal Post processing in laser powder bed fusion processed NiFeMo-based soft magnet, Additive Manufacturing 32 (2020) 101079.

27- K.L.I, Z.Zheng, X. Hung, G. Zhao, J. Feng, J. Zheng, Equilibrium, Kinetic and Thermodynamic Studies on the Absorption of 2-nitroaniline onto activated carbon prepared from cotton stack fibre, J. Hazard. Mater, 166 (2009) 213.

28- F. Nilsén, I. F. Ituarte, M. Salmi, J.Partanen, S.P. Hannula, Effect of process parameters on non-modulated Ni-Mn-Ga alloy manufactured using powder bed fusion, Additive Manufacturing 28 (2019) 464–474

29- E. Patrick. C. N Onukwuli, D. O. Ejikeme, M. Ebere, Optimization of Chemical Treatment Conditions for Adenia Lobata Fiber Using CCD, Inter. J. Eng. Innov. Tech., 4(2014) 23.

30- R. Abdallah, S. L. Soo, R. Hood, The influence of cut direction and process parameters in wire electrical discharge machining of carbon fibre–reinforced plastic composites, Int J Adv Manuf Technol 113 (2021) 1699

31- J. Zou, Y. Gaber, G. Voulazeris, S. Li, L. Vazquez, L.F. Liu, M.Y. Yao, Y.J. Wang, M. Holynski, K. Bongs , M.M. Attallah, Controlling the grain orientation during laser powder bed fusion to tailor the magnetic characteristics in a Ni-Fe based soft magnet, Acta Materialia 158 (2018) 230.

32- C. Bennati, L. Gozzelino, E. S. Olivetti, V. Basso, Heterogeneous nucleation and heat flux avalanches in $La(Fe, Si)_{13}$ magnetocaloric compounds near the critical point, Appl. Phy. Lett. 109 (2016) 231904 .

33- M. M. Attallah, R. Jennings, X. Wang, L. N. Carter, Additive manufacturing of Ni-based superalloys: the outstanding issues, Mater. ReS. Bull. 41 (2016) 758.

34- J. Ma, B. Franco, G. Tapia, K. Karayagiz, L. Johnson, J. Liu, R. Arroyave, I. Karaman, A. Elwany. Spatial control of functional response in 4D-printed active metallic structures. Sci. Rep. 7 (2017) 46707.

35- D. Tomus, T. Jarvis, X. Wu, J. Mei, P. Rometsch, E. Herny, Controlling the microstructure of Hastelloy-X components manufactured by selective laser melting, Phys. Proc. 41 (2013) 816.

36- O. Glushko , A. Funk, V. M.Kiener, P. Kraker, M. Krautz, J. Eckert, A. Waske, Mechanical properties of the magnetocaloric intermetallic $LaFe_{11.2}Si_{1.8}$ alloy at different length scales, Acta Materialia 165 (2019) 40.

37- L.J. Gibson and M.F. Ashby, Cellular Solids: Structure and Properties, Cambridge University Press (1997).

38- M. Leary, M. Mazur, H. Williams, E. Yang, A. Alghamdi, B. Lozanovski, X. Zhang, D. Shidid, L.F.Sternahl, G. Witt, I. Kelbassa, P. Choong, M. Qian, M. Brandt, Inconel 625 lattice structures manufactured by selective laser melting(SLM): Mechanical properties, deformation and failure modes, Mater.& Design 157 (2018) 179.

39- H. Hassanin, L. Finetb, S. C. Cox, P. Jamshidi, L.M. Grover, D. E.T. Shepherd, O. Addison, M. M. Attallah, Tailoring selective laser melting process for titanium drug-delivering implants with releasing micro-channels, Additive Manufacturing 20 (2018) 144.

40- K. Irisawa, A. Fujita, K. Fukamichi, Y. Yamazaki, Y. Iijima, E. Matsubara, Change in the magnetic state of antiferromagnetic $La(Fe_{0.88}Al_{0.12})_{13}$ by hydrogenation, J. Alloys Compds 316 (2001) 70.

41- L. Yang, Z. Zhou, J. Qian, X. Ge, J. Li, Q. Hu, J. Li, Peritectic Solidification Path of the $La(Fe,Si)_{13}$ Phase in Dual-Phase Directionally Solidified La-Fe-Si Magnetocaloric Alloys Metall. Mater. Trans. A 48 (2017)4229.

42- Z. Hu, B. Bo, S. Puji, F. Bin, L. Y.,C. Yongqin, Phase formation with $NaZn_{13}$structure in metamagnetic $La(Fe_{1-x}Co_x)_{11.9}Si_{1.1}$ compounds, J. Rare Earths 26(2008) 727.

43- F. Song, L. Yi, S. Wei , Y. Xueping, C. Yongqin, Y. Rongchang, Y. Kang, Influence of silicon and carbon elements on formation of 1:13 phase and microstructure in $LaFe_{13-y}Si_y$ compounds, J. Rare Earths 30 (2012) 1225.

44- K. Niitsu, R. Kainuma, Phase equilibria in the Fe-La-Si ternary system, Intermetallics 20 (2012) 160-169.

45- V. Raghavan, Fe-La-Si (Iron-Lanthanum-Silicon), J. Phase Equilibria 22 (2001) 158-159.

46- M. Jasinski, J. Liu, S. Jacobs, C. Zimm, La,,Fe,Co,Si…13 bulk alloys and ribbons with high temperature magnetocaloric effect, J. Appl Phy. 107 (2010) 09A953.

47- T. Yildiz, N. Kati, and A.K. Gur, The Effect of Sintering Temperature on Microstructure and Mechanical Properties of Alloys Produced by Using Hot Isostatic Pressing Method, J. Alloys Compd., 737 (2018) 8.

48- F. Yang, H. Wang, L. You, A. A. Volinsky , C. Zhang, Z. Guo, Y. Sui, Performance of Nd-Fe-B Magnets Fabricated by Hot Isostatic Pressing and Low-Temperature Sintering, JMEPEG 28 (2019)273.

49- C. Li, H. Ruan, D. Chen, K. Li, D. Guo, B. Shao Effect of heat treatment on the microstructure and properties of Ni based soft magnetic **alloy** Microsc. Res. Tech., 8 (2018) 1-7.

50- M. Garibaldi , I. Ashcroft , N. Hillier , S.A.C. Harmon , R. Hague, Relationship between laser energy input, microstructures and magnetic properties of selective laser melted Fe-6.9%wt Si soft magnets, Mater. characterization 143 (2018) 144.

51- D Wang, C Song, Y Yang, Y Bai, Investigation of crystal growthmechanism during selective laser melting and mechanical property characterization of 316L stainless steel parts, Materials and Design 100 (2016) 291–299.

52- X.C. Zhong, D.R. Peng, X.T. Dong, J.H. Huang, H. Zhang, Y.L. Huang, S.M. Wu, H. Y. Yu, W.Q. Qiu, Z.W. Liu, R.V. Ramanujan, Improvement in mechanical and magnetocaloric properties of hot-pressed La(Fe,Si)13/La70Co30 composites by grain boundary engineering Materials Science and Engineering B 263 (2021) 114900

53- K. Lowe, J. Liu, K. Skokov, J. D. Moore, H. Sepehri-Amin, K. Hono, M. Katter, O. Gutfleisch, The effect of the thermal decomposition reaction on the mechanicaland magnetocaloric properties of La(Fe,Si,Co)13 Acta Mater. 60 (2012) 4268.

54- H. Zhang, Y. J. Sun, Y. W. Li, Y.Y. Wu, Y. Long, J. Shen, F. X. Hu, J. R. Sun, B. G. Shen Mechanical properties and magnetocaloric effects in La(Fe, Si)13 hydrides bonded with different epoxy resins JOURNAL OF APPLIED PHYSICS 117, (2015) 063902.

55- F. Wang, J. Zhang, Y. F. Chen, G.J. Wang, J. Sun, S. Zhang, B. Shen, Spin-glass behaviour in $La(Fe_{1-x}Mn_x)_{11.4}Si_{1.6}$ compounds, Phys. Rev. B 69, (2004) 094424.

56- Beichner and Serway. Physics for Scientists & Engineers with Modern Physics. 5th ed. Orlando: Saunders College, 2000: 963.

57- S. Fujieda A. Fujita, K. Fukamichi, Y. Yamazaki, and Y. Iijima, Giant isotropic magnetostriction of itinerant-electron metamagnetic $La(Fe_{0.88}Si_{0.12})_{13}H_y$ compounds, Appl. Phys. Lett. 79 (2001) 653.

58- Z. X. Tang, X. H. Deng, G. C. Hadjipanayis, V. Papaefthymiou and D Sellmyer, Structural and magnetic properties of LaFe/sub 13-x/Si/sub x/ nitrides, J. IEEE. Trans. Magn. 29 (1993) 2839

59- L. Jia, J.R. Sun, J. Shen, B. Gao, T.Y. Zhao, H.W. Zhang, F.X. Hu, B.G. Shen, Influence of interstitial and substitutional atoms on the crystal structure of $La(FeSi)_{13}$, J Alloys Compds 509 (2011) 5804.

60- A. Fujita, S.Fujieda, K.Fukamichi, Influence of hydrogenation on the electronic structure and the itinerant-electron metamagnetic transition in strong magnetocaloric compound $La(Fe_{0.88}Si_{0.12})_{13}$, J. Magn. Magn. Mater. 321 (2009) 3553.

61- X.J. Liu, Z.Q. Li, A. Yu , M.L. Liu, W.R. Li, B.L. Li, P. Wu, H.L. Bai, E.Y. Jiang, Magnetic, electrical transport and electron spin resonance studies of Fe-doped manganite $LaMn_{0.7}Fe_{0.3}O_{3+d}$, J. Magn. Magn. Mater. 313(2007) 354.

62- G. Venkataiah and P.V. Reddy, J. Magn. Magn. Mater. 285 (2005) 343

63- F. X. Hu, I. Max, A. M. Tishin, J. R. Sun, G. J .Wang, Y. F. Chen, F. Wang, Z. H. Cheng, B. G. Shen. Direct measurements of mag-netocaloric effect in the first-order system $LaFe_{11.7}Si_{1.3}$. J. Appl. Phys., 93 (2003) 5503.

64- C. Xiang, C. Yungui, T. Yongbai, Influence of iron on phase and magnetic property of the $LaFe_{11.6}Si_{1.4}$ compound, J. Rare Earths 29 (2011) 354.

65- X.Miao , W. Wang, H. Liang2, F. Qian, M. Cong, Y. Zhang, A. Muhammad, Z. Tian, F. Xu, Printing (Mn,Fe)2(P,Si) magnetocaloric alloys for magnetic refrigeration applications, J. Mater. Sci. 55 (2020)6660.

66- S.K. Banerjee, Phys. Lett., 12 (1964) 67.

67- J. Y. Law, V. Franco, L. M. Moreno-Ramírez, A. Conde1, D. Y. Karpenkov, I.Radulov, K. P. Skokov, O. Gutfleisch, A quantitative criterion for determining the order of magnetic phase transitions using the magnetocaloric effect Nature Communications 9 (2018) 2680.

68- B.G. Shen, J.R. Sun, F.X. Hu, H.W. Zhang, Z.H. Cheng. Recent Progress in Exploring Magnetocaloric Materials, Adv. Mater. 21 (2009)4545.

69- P. Nova´k , M. Marysˇko, M. M. Savosta , A. N. Ulyanov, Crossover between the second- and first-order magnetic transition in ferromagnetic manganites, Phy. Rev. B 60 (1999) 6655.

70- Shen, T. D., Schwarz, R. B., Coulter, J. Y. & Thompson, J. D. Magnetocaloric effect in bulk amorphous Pd40Ni22.5Fe17.5P20 alloy. J. Appl. Phys. 91, 5240–5245 (2002).

71- L.M. Moreno-Ramírez , C. Romero-Mu~niz, J. Y. Law, V. Franco, A. Conde, I. A. Radulov F. Maccari, K. P. Skokov, O. Gutfleisch, Tunable first order transition in La(Fe,Cr,Si)13 compounds: Retaining magnetocaloric response despite a magnetic moment reduction Acta Materialia 175 (2019) 406e414.

72- P.MH, Tian SB, Y. SC, Ul. AN, Magnetic and magnetocaloric properties of $La_{0.7}Ca_{0.3-x}Ba_xMnO_3$ compounds. J. Magn. Magn. Mater. 256 (2003) 306.

73- J. Liu, J. D. Moore, K. P. Skokov, M. Krautz, K. Lowe, A. Barcza, M. Katter, and O. Gutfleisch, Exploring La(Fe,Si)13-based magnetic refrigerants towards application Scr. Mater. 67 (2012)584.

74- I. A. Radulov, K. P. Skokov, D. Y. Karpenkov, T. Braun, O. Gutfleisch, Polymer-Bonded $La(Fe,Mn,Si)_{13}H_x$ Plates for Heat Exchangers, IEEE Trans. Magn. 51 (2015) 11.

75- K Kempen, B Vrancken, S Buls, L Thijs, J.V. Humbeeck, J-P Kruth. Selective Laser Melting of Crack- Free High Density M2 High Speed Steel Parts by Baseplate Preheating. J. Manuf. Sci. Eng. 136 (2014)061026.